JGR Oceans

RESEARCH ARTICLE
10.1029/2019JC015119

Key Points:
- Sedimentary inorganic particulate iron can be transported further offshore from coastal regions than its dissolved counterpart
- Dissolution of sedimentary inorganic particles noticeably increases the dissolved iron in remote areas
- Sedimentary inorganic particulate iron then affects the iron limitation patterns of phytoplankton growth, thereby modifying its distribution

Correspondence to:
H. Beghoura and T. Gorgues,
houda.beghoura@univ-brest.fr;
thomas.gorgues@ird.fr

Citation:
Beghoura, H., Gorgues, T., Aumont, O., Planquette, H. F., Tagliabue, A., & Auger, P.-A. (2019). Impact of inorganic particles of sedimentary origin on global dissolved iron and phytoplankton distribution. *Journal of Geophysical Research: Oceans*, *124*, 8626–8646. https://doi.org/10.1029/2019JC015119

Received 4 MAR 2019
Accepted 23 OCT 2019
Accepted article online 7 NOV 2019
Published online 8 DEC 2019

Impact of Inorganic Particles of Sedimentary Origin on Global Dissolved Iron and Phytoplankton Distribution

H. Beghoura[1], T. Gorgues[1], O. Aumont[2], H.F. Planquette[3], A. Tagliabue[4], and P.-A. Auger[1,5]

[1]Université de Brest, CNRS, IRD, Ifremer, Laboratoire d'Océanographie Physique et Spatiale, IUEM, Brest, France, [2]Sorbonne Université, UPMC Université Paris VI, CNRS, IRD, MNHN, UMR7159 LOCEAN-IPSL, Paris, France, [3]Laboratoire des Sciences de l'Environnement Marin, CNRS, UBO, IRD, Ifremer, Plouzané, France, [4]Department of Earth, Ocean, and Ecological Sciences, School of Environmental Sciences, University of Liverpool, Liverpool, UK, [5]Instituto Milenio de Oceanografía and Escuela de Ciencias del Mar, Pontificia Universidad Católica de Valparaíso, Valparaíso, Chile

Abstract Iron is known to be the limiting nutrient for the phytoplankton growth over ~40% of the global ocean and to impact the structure of marine ecosystems. Dissolved iron (DFe) is assumed to be the only form available to phytoplankton while particulate iron (PFe) has mostly been considered for its role in the biogenic iron remineralization and induced scavenging. Therefore, most studies focused on the nature of DFe external sources to the ocean (i.e., eolian dust, riverine fluxes, hydrothermal sources, and sediment) and their quantification, which still remain uncertain. Among these external sources, the sedimentary sources have been shown to be underestimated. Moreover, the iron supply from sediments has been documented to be often larger in the particle fraction. Here we test the impacts of an iron sediment source of inorganic particulate iron (PFe_{Inorg}) on global DFe and phytoplankton distribution. We use experimentally acquired knowledge to test a parameterization of a PFe_{Inorg} pool in a global biogeochemical model and compare with published indirect estimation. Depending on the parameterization of its dissolution and sinking speed, the PFe_{Inorg} can noticeably enrich water masses in DFe during its transport from the sediment to the open ocean, notably in regions not usually accessible to external DFe inputs. Indeed, the fact that DFe is prone to scavenging reduces the impact of equivalent Fe inputs from sediments in the dissolved form in those regions far from the sediment sources. PFe_{Inorg} thereby has the potential to fuel the phytoplankton growth in offshore regions impacting the coastal-offshore chlorophyll gradient.

1. Introduction

In the ocean, photoautotrophs' productivity is known to be limited by the availability of macronutrients and micronutrients. Among those nutrients, iron (Fe) is acknowledged to limit primary production over ~40% of the ocean (Boyd & Ellwood, 2010; Geider & La Roche, 1994; Moore et al., 2013) and consequently the efficiency of atmospheric carbon ocean uptake (e.g., Aumont & Bopp, 2006; Buesseler et al., 2004; Smetacek et al., 2012). Moreover, iron supplies have been demonstrated to have a regulatory effect on the phytoplankton community structures (Hare et al., 2005; Hutchins et al., 2002). Small changes in seawater iron concentrations can therefore have a profound impact on the growth of phytoplankton, affecting the productivity of ecosystems, the structure of the trophic food web, and the efficiency of carbon sequestration. However, to date, there are still substantial uncertainties in the iron biogeochemical cycle, including the magnitude and the physicochemical form of the external iron sources to the ocean.

Indeed, external sources of iron such as dust deposition from the atmosphere (Jickells, 2005), inputs from the sediments (Chase et al., 2005; Dale et al., 2015; Elrod et al., 2004; Homoky et al., 2013; Johnson et al., 1999), riverine fluxes (Da Cunha & Buitenhuis, 2013), and hydrothermal inputs (Tagliabue et al., 2010) deliver iron in a variety of chemical and physical forms, whose influence on the dissolved iron (DFe) pool is still poorly constrained (Raiswell & Canfield, 2012).

Over the last two decades, dust deposition has been considered to be the main source of Fe to the open ocean (Archer & Johnson, 2000; J. Keith Moore et al., 2002, 2004). However, observations in the Pacific (Lam &

Bishop, 2008), Atlantic (Milne et al., 2017), and Southern (Van Der Merwe et al., 2015) Oceans are questioning the relative importance of other sources of marine iron, such as iron fluxes from sediments (Dale et al., 2015; Tagliabue et al., 2014). Those latter fluxes include a source of DFe released through sediment reductive mobilization and resuspension of particles of iron (mostly in the form of iron hydroxide, Fe $(OH)_3$). This aforementioned resuspension of particles from continental slopes and margins has been identified as a potentially underestimated source of iron (Jeandel et al., 2011; Lam & Bishop, 2008). Indeed, over the continental slopes and margins most of the iron is actually present in the form of resuspended particulate iron (e.g., Milne et al., 2017).

Since the operationally defined dissolved iron (DFe, which is the sum of truly dissolved and colloidal iron) was traditionally assumed to be the only form available to phytoplankton and bacteria, most studies have focused on the supply of DFe to the ocean. The role of the particulate fraction (PFe) as an external source of bioavailable iron has then been largely ignored. Indeed, to date, particulate iron has mostly been viewed for its role in the biogenic iron remineralization, the scavenging, and aggregation processes (Ohnemus & Lam, 2015). This traditional view has been challenged by modeling studies (e.g., Gorgues et al., 2009), and more recently, experiments (e.g., Cheize et al., 2019; Jeandel & Oelkers, 2015) have stressed the role of lithogenic particles dissolution as a slow release of DFe. Thus, it has been suggested that the lithogenic particles from ocean margins may act as a "continuous fertilizer" impacting open ocean phytoplankton communities. Indeed, the exchange between the particulate and dissolved fractions results in a net flux from PFe to DFe (Abadie et al., 2017; Cheize et al., 2019; Homoky et al., 2013; Johnson et al., 1997; Labatut et al., 2014) inducing a source of DFe that potentially sustains productivity in shallow coastal waters but also in the open ocean.

During the last decade, several global scale models have been developed including an explicit representation of the iron cycle (see Tagliabue et al., 2016, and references therein). In an intercomparison exercise of those models performance (SCOR working group: FeMIP), Tagliabue et al. (2016) have shown that models were able to explain less than 30% of the observed iron spatial distribution over the global ocean. One part of the explanation for this relatively poor score could be the absence of lithogenic inorganic particulate iron of sedimentary origins (PFe_{Inorg}) in those models. Indeed, models that consider particulate iron's pools take into account at best two classes of solely biogenic particulate iron (hereafter PFe_{bio}: living and dead organic matter; Tagliabue et al., 2016). To our knowledge and despite the aforementioned evidences, no ocean biogeochemical model is yet considering sources of inorganic particulate iron of sedimentary origin.

In this context, the aim of this study is to use new experimentally acquired knowledge of the significance of particulate iron dissolution from sedimentary sources to assess its first-order impact on global ocean biogeochemistry. To this end, we propose a modeling approach investigating the effect of the dissolution of the lithogenic inorganic particulate iron of sedimentary origin to the open ocean iron inventory and phytoplankton biomasses. This dissolution, which represents a potential source of DFe, is parameterized based on previously published estimates of dissolution obtained from (i) laboratory experiments (Cheize et al., 2019) and (ii) in situ observations.

2. Materials and Methods

2.1. Model Configuration

In this study, we used a model configuration exactly similar to the one used in Aumont et al.'s (2015) study. Therefore, only the main aspect of this configuration, needed to comprehend our modeling exercise, are recalled here (for further details, please refer to Aumont et al. (2015)). Briefly, we used ocean global seasonal climatologies from an ocean dynamical state that have been simulated using the ocean physical model ORCA2-LIM in its version 3.2 (Madec, 2008). The horizontal resolution of this physical model was set at 2° with a finer meridional resolution of 0.5° in the equatorial domain. Thirty vertical layers were used with an increased vertical thickness from 10 m at the surface to 500 m at 5,000 m. These simulated ocean state climatologies were then used to force the Pelagic Integration Scheme for Carbon and Ecosystem Studies (PISCES) ocean biogeochemical model (Aumont et al., 2015) over 300-year time periods.

The PISCES model simulates the biogeochemical cycles of carbon (C) and of the main nutrients (phosphate (P), nitrogen (N), iron, and silicon (Si)) as well as the lower trophic levels of marine ecosystems. The latter

comprise four living compartments: two phytoplankton size groups corresponding to nanophytoplankton and diatoms and two zooplankton size classes (microzooplankton and mesozooplankton). In PISCES, a mixed Monod-quota formulation has been preferred with a fixed stoichiometry of C/N/P and variable quotas for iron. Growth rates of phytoplankton are then limited by external nutrients concentrations (N, P, Si) and by internal iron availability. The chlorophyll (Chl) to carbon ratio for the two phytoplankton groups is parameterized using the photo-adaptive model of Geider et al. (1997), while the Fe and Si phytoplankton contents are computed as a function of external concentrations and light levels. For all 300-year simulations, phosphate, oxygen, nitrate, and silicic acid distributions have been initialized with concentrations derived from observed climatologies (Garcia et al., 2010). Iron concentrations have been set everywhere to 0.6 nmol/L as in Aumont et al. (2015), while initial values for dissolved inorganic carbon and alkalinity are taken from the OCMIP guidelines (Orr, 1999).

2.2. Classic PISCES Iron Cycle

The PISCES model has been widely used in a variety of studies focusing on the iron cycle at global (Aumont & Bopp, 2006; Tagliabue et al., 2009, 2010), regional (Gorgues et al., 2009; Gorgues et al., 2010; Slemons et al., 2009), and local scale (Borrione et al., 2014). The "classic" PISCES iron cycle (detailed in Figure 1) relies on two dissolved iron forms: the free iron (Fe′) and the ligand-complexed iron (FeL), both of them considered as equally bioavailable. Only one ligand pool is used with a fixed and uniform concentration set at 0.7 nmol/L (Aumont et al., 2015). Furthermore, we assume that 50% of the complexed iron (FeL) constitutes the colloidal iron (Fe_{coll}). The Fe_{coll} is affected by aggregation with dissolved and particulate organic matter. With this approach, inorganic dissolved free form (Fe′) is assumed to be the only form of iron susceptible to scavenging, a potentially important iron sink (Ye et al., 2009), which refers to a transfer of dissolved iron (DFe) to the particulate pool. These particles then settle to the ocean floor and their iron content is then permanently removed from the ocean by this process. As suggested by observational studies (e.g., Honeyman & Santschi, 1989; Parekh et al., 2004), the scavenging rate of iron in PISCES is made dependent upon the different types of biogenic particles and the lithogenic particles originating from dust deposition. The iron scavenged by biogenic particles is then routed in the particulate organic matter and susceptible to dissolve back in the water column. Moreover, in the model, scavenging is enhanced when DFe concentration exceeds the total ligand concentration, as it is done in other biogeochemical models (e.g., Dutkiewicz et al., 2005; Moore et al., 2004).

External supply of iron to the ocean is achieved through atmospheric dust deposition, river discharge, hydrothermal vents, and reductive mobilization from marine sediments (for an exhaustive description of the implementation of these sources in PISCES, see Aumont et al. (2015)). The modeled sediment external iron sources add iron to the ocean in its dissolved form only. The sediment iron source in PISCES is considered constant over time and is made vertically variable in order to mimic the effect of oxygen levels in the sediments (i.e., the reductive mobilization of iron from marine sediments). Indeed, anoxic sediments (i.e., those one would find in the presence of abundant organic matter) are likely to release more iron to seawater (Elrod, Berelson, Coale, & Johnson, 2004; Elrod, Berelson, Coale, Johnson, Berelson, et al., 2004). The depth of each grid cell is then used as a proxy of the sediment oxygenation (Middelburg et al., 1996) resulting in an overall decrease toward greater depth of the iron flux from its maximum value. This value of DFe flux has been set at $2\ \mu mol\ m^{-2}\ d^{-1}$, a value obtained by Moore and Braucher (2008) and Aumont and Bopp (2006) by optimizing their biogeochemical modeling results with global Fe data sets and which is in the range of published values (Dale et al., 2015; Elrod, Berelson, Coale, & Johnson, 2004; Elrod, Berelson, Coale, Johnson, Berelson, et al., 2004; Johnson et al., 1999).

A comparison of the simulated chlorophyll *a* (a proxy of primary producer's biomass) for a standard PISCES simulation (hereafter referred as "D2" and using the classic iron cycle described in this section) and observations from satellite (SeaWiFS) is shown in Figure 2 to document the overall agreement between the model and the data on large-scale oceanic patterns. Note that the purpose of this paper is not to identify and discuss the various biases of the model as most of this work has been done in the study of Aumont et al. (2015). Rather, we would like to draw the reader attention on specific patterns of this standard simulation, such as the weaker modeled chlorophyll maximum than observed in the equatorial Pacific, or the weaker than observed extension of the Islands Mass Effect (hereafter "IME" (Doty & Oguri, 1956), which is visible through the chlorophyll plumes downstream islands) noticeably in the Southern Ocean.

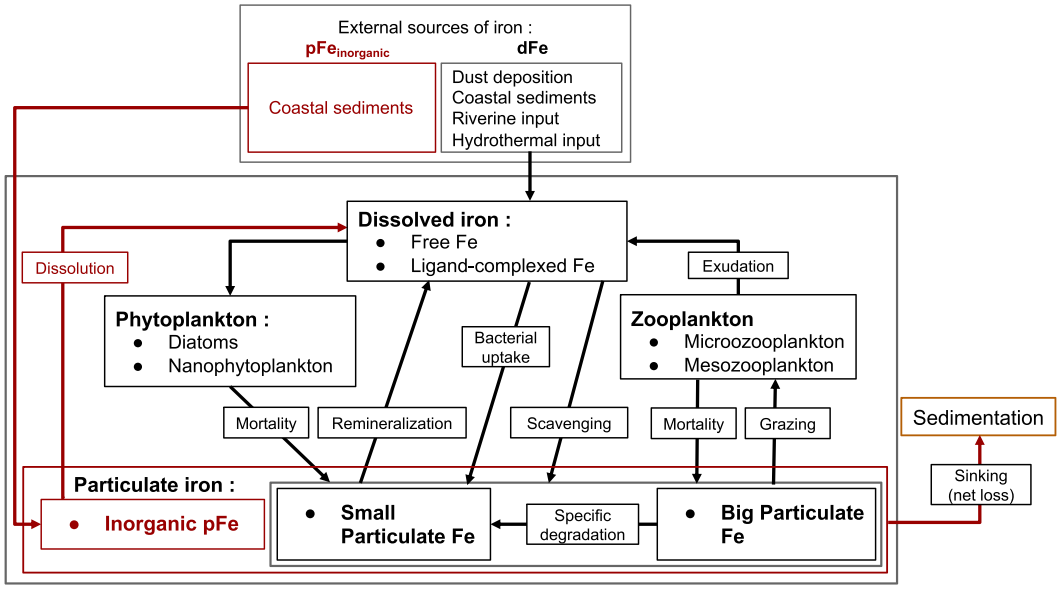

Figure 1. Schematic of the iron cycle in the biogeochemical model PISCES (Aumont et al., 2015), used in this study. Additions made to the "classic" PISCES cycle (in black) appear in red on this schematic.

2.3. In Situ Data

Thanks to international programs such as GEOTRACES (www.geotraces.org), several recent cruises allowed further documentation of dissolved and particulate iron concentrations, among other trace elements. In addition to the modeling results, we used in this paper an updated compilation of measurements gathered in a database of DFe for the global ocean (http://pcwww.liv.ac.uk/~atagliab) that has been published in Tagliabue et al. (2012). The original database gathered >13,000 measurements to which 9,612 recent observations have been added for the purpose of this study. Despite these observational efforts, Figure 3 shows that the spatial distribution of DFe data remains quite sparse. Nevertheless, some large-scale patterns can be identified, such as (i) the high surface DFe concentration in the Atlantic ocean due to the Saharan dust inputs, (ii) an overall increase from the surface toward greater depths, and (iii) a well-marked coastal to offshore regions gradient. Full model results of the simulation D2 (classic PISCES simulation) are presented in Figures 3e and 3f and have also been subsampled at data location and time to illustrate the challenges posed by model-data intercomparison. If D2 is able to broadly represent the large-scale observed patterns of the dissolved iron distribution, either in surface or in subsurface (Aumont et al., 2015; Tagliabue et al., 2016), some noticeable differences remain. Indeed, the D2 simulation displays weaker than observed surface and subsurface dissolved

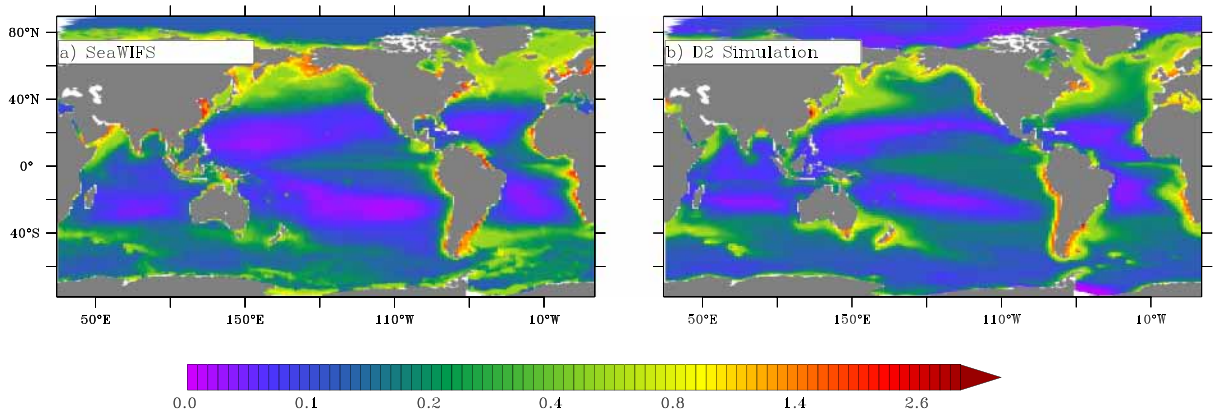

Figure 2. Annually averaged surface chlorophyll concentration (mg/m^3) from (a) SeaWIFS data (https://oceancolor.gsfc.nasa.gov/l3) and (b) the D2 simulation.

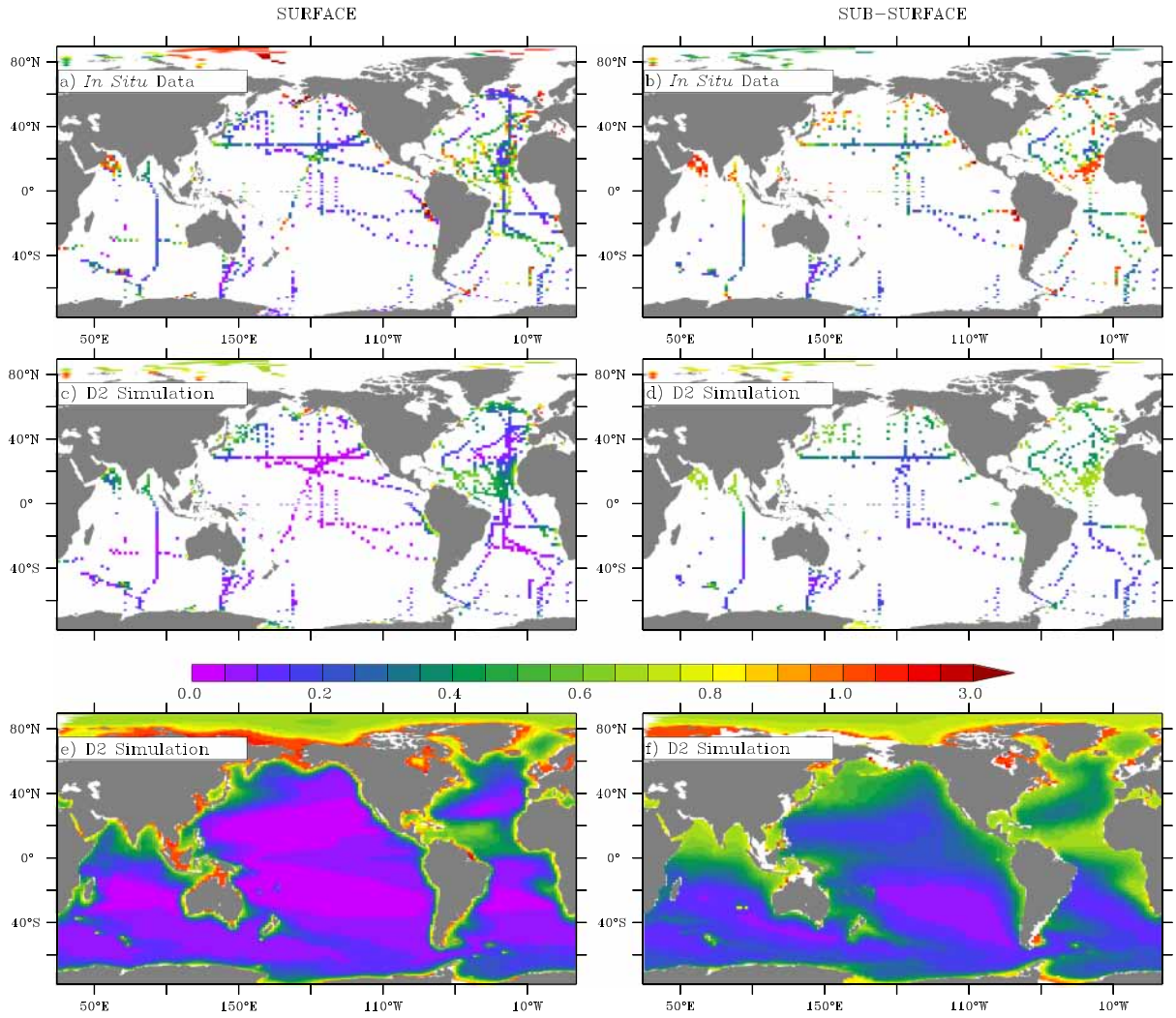

Figure 3. Dissolved iron concentration (in nmol/L) averaged over the (left panel) top 0–100 m and (right panel) between 100 and 500 m, from (a and b) in situ data and (c and d) subsampling at the data locations of the annual mean as simulated in PISCES standard simulation (i.e., D2 simulation). (e and f) Correspond to the same outputs than (c) and (d) but without the data subsampling.

iron concentrations near most of the coastlines, as well as at the southern boundary of the North Atlantic subtropical gyre, in the Arabian sea, at the equator in the Pacific warm pool, and in the Southern ocean downstream the Drake passage and Southern islands (i.e., South Georgia and South Sandwich, Bouvet islands). However, the most striking and globally noticeable difference is a modeled too steep large-scale (~1,000 km) gradient between high coastal and low open ocean DFe concentrations.

An evaluation of our biogeochemical model skill in reproducing the distribution of the DFe observed concentrations has already been partially done in Tagliabue et al. (2016) and Aumont et al. (2015). As already stated in section 1, the aim of this study is not solely to improve the realism of the model but rather to document the effect of processes that we know are missing in biogeochemical models. The objective of Figure 3 is thus to provide a reference state to which will be compared the other simulations proposed in this study.

2.4. Inorganic Particulate Iron of Sedimentary Origin

To investigate the potential impacts of particulate iron from sedimentary sources, the biogeochemical PISCES model was modified to add a new compartment of inorganic particulate iron (PFe_{Inorg}; see Figure 1). Once released by the sediment, its temporal evolution is dependent on dissolution and sinking (see equation 1).

$$\frac{\partial \mathrm{PFe_{Inorg}}}{\partial t} = -w_{\mathrm{PFe_{Inorg}}} \frac{\partial \mathrm{PFe_{Inorg}}}{\partial z} - \lambda_{\mathrm{PFe_{Inorg}}} \mathrm{PFe_{Inorg}} \quad (1)$$

In this latter equation, $w_{PFe_{Inorg}}$ and $\lambda_{PFe_{Inorg}}$ are, respectively, standing for the vertical sinking speed and the dissolution rate of the PFe_{Inorg}. The source of our PFe_{Inorg} is predominantly located on continental shelves which are generally very productive regions where biogenic particle concentrations are high. The DFe scavenging loss onto PFe_{Inorg} has then not been considered in this study.

As for now, and despite an increasing number of recent observations (e.g., Annett et al., 2017; Gourain et al., 2018; Planquette et al., 2011, 2013), very few data are yet available to directly parameterize those processes in global models. Therefore, in our study, the vertical speed ($w_{PFe_{Inorg}}$) has been computed from the stokes law applied to a particle size of 3 μm, as some studies (Lam et al., 2006, 2012) reported particles containing iron (e.g., Fe-silicate particles, hydroxide, oxyhydroxide, pyrite) with a diameter ranging from 0.8 to 4 μm. However, Ohnemus and Lam (2015) showed, in a North-Atlantic section, that small iron particles (between 0.8 and 51 μm) can potentially be aggregated within large particles (>51 μm). They found that the large size fraction represented ~50% (and sometimes up to 80% locally) of total particulate iron in surface ocean while in the deep ocean it decreases to less than 20% (see their Figure 5). Therefore, most of the iron particles are indeed constituted of small iron particles and account for most of the particle mass in the ocean (while large particles transport most of the vertical flux; see Lam & Marchal, 2015, and references therein). However, the relative abundance of aggregates advocates to also consider larger sinking speeds. Therefore, we consider vertical sinking speeds corresponding to particle sizes ranging from 3 to larger particles of 10 μm to take into account a potential effect of aggregation. The sinking velocities of those particles are respectively 0.2 and 2 m/day. In addition to these values, a "no sinking speed" ($w_{PFe_{Inorg}} = 0$ m/day) test case has also been ran. Our values (0, 0.2, and 2 m/day) are bracketing published values (Lam et al., 2006, 2012) that are ranging from ~0.1 to ~0.9 m/day with the most plausible value at 0.2 m/day.

To set the dissolution rate ($\lambda_{PFe_{Inorg}}$), we benefited from the results of dissolution experiments conducted by Cheize et al. (2019), which used, for the first time, realistic suspended particle concentrations and were performed under trace metal clean conditions. In those dissolution experiments, particles of sediments from different origins were kept in seawater for a 14-month incubation period at a constant temperature of 15°C. Regular measurements of the dissolved iron concentration were conducted during the incubation period. Dissolution rates computed in Table 1 are then calculated from the leachable iron concentrations (unpublished data; see Table 1) and the published DFe concentrations from Cheize et al. (2019). In the latter study, dissolution is not monotonic for any of the sediment samples. The minimum dissolution rates for all sediment types are observed at the beginning of the time series with virtually no dissolution for the first month. Then, the dissolution rates do vary significantly. Opal rich sediments show the fastest dissolution rates, which reach a maximum of 3.7×10^{-4} day observed between day 57 and day 71. Data from the Cheize et al.'s (2019) experimental study then suggest a range of dissolution rates from 4.2×10^{-5} to 3.7×10^{-4} day depending on the nature (calcite, basalt, and opal) of the sedimentary particles, that all originate from the Kerguelen area. Those values are significantly lower than the indirect estimation of 6×10^{-3} day inferred by Slemons et al. (2012) from equatorial Pacific in situ observations.

Finally, to the author's knowledge, there is no published observation of the PFe_{Inorg} fluxes from the sediments to the ocean. However, measured concentrations of particulate iron close to the coast are often 10 times greater than DFe concentrations (e.g., Bowie et al., 2015; Van Der Merwe et al., 2015; Planquette et al., 2007, 2009, 2013; Slemons et al., 2012). These observations suggest that the particulate iron flux from sediment resuspension may be higher than the DFe flux (maximum value set at 2 μmol m^{-2} d^{-1} in our model), an assumption already made by Croot and Hunter (1998) and Johnson et al. (1999). Thus, we chose to parameterize the PFe_{Inorg} iron sediment flux with a maximum value set at 8 μmol m^{-2} d^{-1}. The latter value allows the model to roughly simulate the observed difference close to the coast of one order of magnitude between the DFe concentration (~1 nmol/L) and the particulate one (~10 nmol/L). Moreover, the particulate iron source is driven by sediment resuspension processes and therefore should be higher in the surface and subsurface ocean where the circulation is more energetic than in the deep ocean. Therefore, we chose to parameterize the PFe_{Inorg} iron sediment flux with a vertical attenuation exactly similar to the one used for the DFe flux (i.e., higher DFe fluxes related to the lower oxygen concentrations of the sediments lying within surface ocean productive layers; see section 2.2).

Table 1
Additional Data to the Cheize et al. (2019) Experiments Used to Compute the Dissolution Rates of the PFe_{Inorg}. and Corresponding Mean and Maximum Dissolution Rate Observed During the 423 Days of the Dissolution Experiment

Sediment types	Opal (A3 in Cheize et al. (2019))	Opal and calcite (C11 in Cheize et al. (2019))	Basalt (C1 in Cheize et al. (2019))
Seawater in reactor (L)	11.6	11.5	11.6
Leachable iron introduced in reactor (mol)	9.0×10^{-7}	2.9×10^{-7}	7.1×10^{-7}
Mean dissolution rate (day)	1.2×10^{-4}	8.8×10^{-5}	4.2×10^{-5}
Maximum dissolution rate (day)	3.7×10^{-4}	2.2×10^{-4}	8.6×10^{-5}

2.5. Experimental Setup

Our study performed simulations differing in the parameterization of the iron flux from the sediments (Table 2): (i) a classic PISCES simulation with 2-μmol m^{-2} d^{-1} DFe sediment flux hereafter named "D2", (ii) a simulation with an increased DFe flux from 2 to 10 μmol m^{-2} d^{-1} referred as "D10," and (iii) a set of simulations with an iron sediment flux constituted from a lithogenic inorganic particulate iron flux (PFe_{Inorg}) set at 8 μmol m^{-2} d^{-1} and a DFe flux of 2 μmol m^{-2} d^{-1}. In the latter simulations, the overall total coastal iron flux was similar to D10 but distinguished in two iron pools (i.e., particulate and dissolved). Given the large uncertainties on the dissolution rate, three simulations with a PFe_{Inorg} flux were run that differ in the prescribed value of the dissolution rate: the P_{slem} simulation used a dissolution rate of 6×10^{-3} day corresponding to the estimate by Slemons et al. (2012). In P_{med} and P_{min}, dissolutions rates were chosen to bracket the values derived from Cheize et al. (2019) (see Table 1) and were set to 4×10^{-4} and 4×10^{-5} day, respectively. The simulation with an intermediate dissolution rate (i.e., P_{med}) is subsequently used as a reference. In reference to simulation D2, it serves to document the effects of incorporating a sediment source of lithogenic iron compared to the most commonly used parameterization of sediment iron source in biogeochemical models (Tagliabue et al., 2016). However, the total amount of the iron input (of any form) is not consistent between those two latter simulations. Thus, in order to specifically address the role of the inorganic particulate iron phase from sedimentary sources on the production patterns, the simulation

Table 2
List of the Simulations With Their Parameter Values

Simulations Names		Dissolution rate of PFe_{Inorg} (day)	Sinking speed of PFe_{Inorg} (m day^{-1})	PFe_{Inorg} input from sediment (μmol m^{-2} day^{-1})	Dissolved iron input from sediment (μmol m^{-2} day^{-1})	Total iron input (dissolved + particulate) from sediment (μmol m^{-2} day^{-1})
D2					2	2
D10					10	10
P_{slem}	P^{Msink}_{slem}	6×10^{-3}	0.2	8	2	10
	P^{Nosink}_{slem}		0			
	P^{10sink}_{slem}		2			
P_{med}	P^{Msink}_{med}	4×10^{-4}	0.2	8	2	10
	P^{Nosink}_{med}		0			
	P^{10sink}_{med}		2			
P_{min}	P^{Msink}_{min}	4×10^{-5}	0.2	8	2	10
	P^{Nosink}_{min}		0			
	P^{10sink}_{min}		2			

D10, which has the same overall iron input to the ocean than P_{slem}, P_{med}, and P_{min}, has then been used to allow a meaningful comparison.

Our parameterization of lithogenic iron relies on two parameters: the dissolution rate and the sinking speed of lithogenic particulate iron. The sensitivity to the dissolution rate is explored by comparing P_{med}, P_{min}, and P_{slem}. The role of sinking is investigated by prescribing three different sinking speeds for each value of the dissolution rates. In the experiments labeled "Msink," the sinking speed has been set to 0.2 m/day. In "10sink," this speed has been multiplied by 10, that is, 2 m/day. In the "Nosink" experiments, we assume that lithogenic particles do not sink and thus, the sinking speed is set to 0 m/day. Thus, a total of nine simulations have been performed for the model configurations that represent particulate iron of sedimentary origin. Our reference simulation P_{med}^{Msink} used the sinking velocity set at 0.2 m/day. All the simulations and their main characteristics are summarized in Table 2.

3. Results and Discussion

3.1. Iron Inventories

Adding an additional Fe source, PFe_{Inorg}, of course impacts the global inventory of the different forms of iron at a global scale. The extra iron flux in D10 and Pref raises the inventory of total iron at a global scale compared to the D2 simulation (Table 3), but the total iron inventory increase is greatest when part of the iron is added in its particulate form (PFe_{Inorg}). This is due to the fact that DFe is subjected to intense scavenging in the model when its concentration exceeds the ligand concentration of 0.7 nmol/L. In D10, this process results in a net loss of DFe toward biogenic particles. These particles then quickly sink resulting in a net loss of iron for the ocean. As the sinking speed of PFe_{Inorg} particles is lower than for biogenic small and big particles by, respectively, 1 and 2 orders of magnitude, the iron is "retained" in the inorganic particulate phase in $\mathbf{P_{med}^{Msink}}$ (Table 3). Thus, it results in a lower loss of total iron from the ocean in $\mathbf{P_{med}^{Msink}}$ than in D10.

In line with the global total iron inventory, the global DFe inventory displays higher values in the $\mathbf{P_{med}^{Msink}}$ simulation than in D10. This latter inventory hides opposite responses of the deep and surface ocean toward addition of inorganic particulate iron of sedimentary origin. Indeed, the ocean surface productive layers (0–100 m) display almost unchanged DFe concentrations between $\mathbf{P_{med}^{Msink}}$ and D10 (slightly higher in D10), while in the subsurface and in the deep ocean the DFe inventory significantly increases (see Table 3). For these two latter depth intervals, the processes explaining the higher DFe concentration in $\mathbf{P_{med}^{Msink}}$ than in D10 are similar to those invoked previously for the total iron inventory. The increase of the iron flux from the sediments exclusively in its dissolved phase (D10 simulation) induces the DFe concentration to exceed the 0.7-nmol/L threshold near the sediment sources and triggers a noticeable increase of the scavenging. A significant amount of this added iron is then lost close to the source regions through scavenging and vertical settling of biogenic particles. In $\mathbf{P_{med}^{Msink}}$, most of the source of the sedimentary iron is composed of inorganic particulate iron (PFe_{Inorg}), not susceptible to scavenging, that are transported by currents and vertical settling to the subsurface and deep ocean layers while dissolving. The relatively slow dissolution allows a large part of PFe_{Inorg} to reach these depths (almost 90% of the PFe_{Inorg} pool lies deeper than 500 m; Table 3) despite its source being stronger in surface layers. Then, as it dissolves, PFe_{Inorg} adds DFe locally to the water masses explaining the simulated DFe increase. Noteworthy, the dissolution of the PFe_{Inorg} does not reflect on the inventory of the DFe in the top hundred meters of the ocean. Indeed, in this thin productive layers, the dissolution of the iron drive a biomass increase most pronounced for the $\mathbf{P_{med}^{Msink}}$ simulation than for D10 (compared to D2, the biomass increase of PFe_{Inorg} is twice the one of D10). Therefore, the dissolved iron originating from the PFe_{Inorg} dissolution is uptaken more intensively by the higher biomass simulated in $\mathbf{P_{med}^{Msink}}$ than in D10, which explains the weak difference of the surface dissolved iron pool between those two simulations.

3.2. Iron Distribution

In this section, we chose to focus the discussion on the surface and subsurface layers, as differences in spatial patterns between the simulations (with and without the PFe_{Inorg}) may impact the ecosystem.

The spatial distribution of the iron anomaly due to the increased sedimentary iron source with respect to D2 is displayed in Figure 4 in the surface and subsurface layers. As expected, an increase of the DFe is clearly

Table 3
Iron Inventory in the D2, D10, and P^{Msink}_{med} *Simulations in* 10^{11} *mol Over the Productive Layer (0–100 m), the Subsurface (100–500 m), and the Deep Ocean (500–Seafloor)*

Simulations	Total Fe inventory (in 10^{11} mol): dissolved + particulate	DFe inventory in 10^{11} mol				Total PFe inventory (PFe_{Inorg} + PFe_{Bio}) in 10^{11} mol				PFe_{Inorg} inventory in 10^{11} mol (*% of total PFe*)			
	Global	Global	0–100 m	100–500 m	500–seafloor	Global	0–100 m	100–500 m	500–seafloor	Global	0–100 m	100–500 m	500–seafloor
D2	5.69	5.27	0.09	0.57	4.61	0.42	0.02	0.05	0.35				
D10	7.23	6.75	0.14	0.74	5.87	0.49	0.02	0.06	0.41				
P^{Msink}_{med}	16.93	7.13	0.13	0.91	6.09	9.80	1.07	3.01	5.72	9.27 (*95%*)	1.04 (*97%*)	2.95 (*98%*)	5.28 (*92%*)

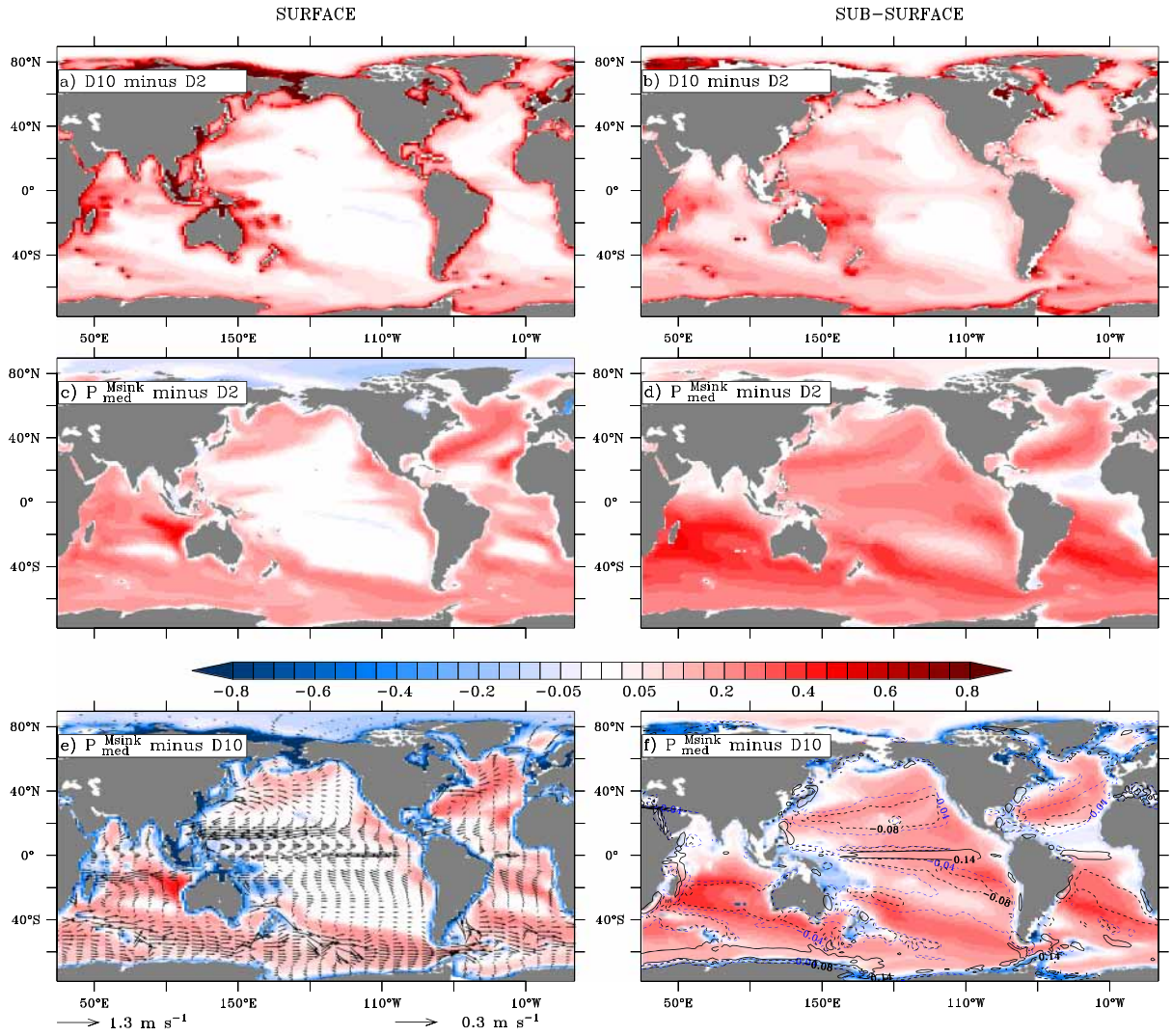

Figure 4. Annual mean dissolved iron anomaly (in nmol/L) averaged over the (left panel) top 0–100 m and (right panel) between 100 and 500 m. (a) and (b) correspond to DFe anomaly that is D10 simulation in reference to the D2 simulation, (c) and (d) P^{Msink}_{med} in reference to D2, and (e) and (f) P^{Msink}_{med} in reference to D10. Surface currents (0–100 m) have been plotted over (e) with vectors. To emphasize the surface circulation patterns two vectors scales have been applied: a vector set at 0.3 m/s between 9°S and 9°N and a vector set at 1.3 m/s poleward. Contours on (f) represent the annual mean of the vertical velocity at 100 m, the dashed blue and black lines correspond to the downward currents (negative velocity), and the continuous black lines correspond to upward currents.

visible globally when compared to D2 either for $\mathbf{P_{med}^{Msink}}$ or D10 (Figures 4a–4d). Increasing the amount of iron released by the sediments, only in its dissolved form (D10 simulation; see Figure 4a), leads to a surface increase of DFe concentration limited to a relatively narrow band near the topography, and occasionally transported slightly offshore when intense surface currents take place (e.g., the Indian Equatorial currents, the Antarctic Circumpolar Current, the Pacific north equatorial countercurrent, and the Kuroshio). The subsurface increase of DFe concentration follows roughly the same patterns than the one described in surface with the noticeable addition of a pattern typical of the Pacific Equatorial Undercurrent (i.e., narrow equatorial band of high DFe; Figure 4b). Conversely, adding iron in its particulate form increases the DFe over a wider area following the topography, either in surface or subsurface (Figures 4c and 4d). Spatial patterns corresponding to the general oceanic circulation (e.g., Gulf Stream, Kuroshio, and subsurface Pacific Equatorial Undercurrent) become also more noticeable with the addition of iron in its particulate form (Figures 4c and 4d).

The direct quantification of the role of particulate iron sourced from the sediments can be seen by comparing the $\mathbf{P_{med}^{Msink}}$ and D10 simulations and is shown in Figures 4e and 4f. In surface (0–100 m), the impact of a PFe_{Inorg} source, compared to a fully DFe source is mostly significant in coastal areas and in regions characterized by intense horizontal currents (Figure 4e; e.g., Gulf Stream, Kuroshio). Yet the DFe concentration is higher in D10 than in $\mathbf{P_{med}^{Msink}}$ in the very first grid cells near the topography. Indeed, the dissolved iron added in D10 is sustaining high concentration in those grid cells. Conversely, in $\mathbf{P_{med}^{Msink}}$, only a fraction of the PFe_{Inorg} is dissolving before being transported away from the topography. Thus, DFe concentrations in those very first grid cells close to the topography mirror the intensity of the DFe sediment sources, which are higher in D10 than in $\mathbf{P_{med}^{Msink}}$.

Further away from the coast, DFe concentrations decrease faster in D10 than in $\mathbf{P_{med}^{Msink}}$ while being transported offshore. This is the result of (i) high scavenging rates in regions characterized by relatively high DFe concentration (i.e., above the aforementioned 0.7-nmol/L threshold) and (ii) low vertical export of PFe_{Inorg} in $\mathbf{P_{med}^{Msink}}$ due to small sinking velocities relative to the surface horizontal currents (i.e., respectively, 0.2 m/day versus 0.1 m/s).

Moreover, coastal regions, where the sediment sources are added, are known to be productive areas (Figure 2) and are therefore characterized by high iron biological uptake, while PFe_{Inorg} is not directly influenced by biological uptake. Consequently, the PFe_{Inorg} can easily escape the sediment source areas while DFe inputs are either scavenged due to DFe concentrations well above the ligand threshold, or uptaken by biology, which limits DFe transport by ocean circulation. Oppositely, PFe_{Inorg} is then transported further offshore while slowly releasing DFe. Therefore, in the surface layer, the impacts of the PFe_{Inorg} on the DFe concentrations mostly mimic the large-scale horizontal circulation (Figure 4e).

Subsurface patterns (100–500 m) of the differences in DFe between the simulations differ from the surface. Indeed, the DFe differences relative to D2 (either for D10 and $\mathbf{P_{med}^{Msink}}$) are higher very near the source regions (closest grid cells to the coastline) in the surface layer (0–100 m) than in the subsurface (Figures 4a and 4c), which is consistent with the vertical attenuation of the iron source (whatever its form) from the surface to the deep ocean. Other differences between the surface and subsurface lie in the distinctive large-scale lateral circulation patterns that transport PFe_{Inorg} farther than DFe (Figure 4f). For example, the enrichment of the EUC by the subsurface western equatorial Pacific is clearly visible on subsurface plots with a stronger increase (compared to D2) in the $\mathbf{P_{med}^{Msink}}$ simulation than in D10. DFe concentrations in $\mathbf{P_{med}^{Msink}}$ also display higher concentrations than D10 below large-scale surface convergence zones. In such areas, surface DFe from the PFe_{Inorg} dissolution is downwelled toward greater depths (Figure 4f). Compared to D10, this increased vertical transport of iron toward the subsurface also reflects on the mode waters, which display higher DFe concentrations in $\mathbf{P_{med}^{Msink}}$ (Figure 4f). Finally, the biological uptake in subsurface is virtually equal to zero leading to a more distant transport of DFe released from the PFe_{Inorg}. It ultimately results in wider areas of DFe increase than in surface.

3.3. Sensitivity of the Simulated Iron Distribution to Model Parameters

As almost no data of the fraction of PFe_{Inorg} that can dissolve in the ocean exist, observations cannot yet be used to evaluate the predicted PFe_{Inorg} distribution. As a consequence, the model parameters cannot be

constrained by such an evaluation. An assessment of the sensitivity of the simulation outputs to the model parameters is thus needed to evaluate the robustness of the impacts of the PFe_{Inorg} on marine iron and phytoplankton biomasses. Therefore, in addition to the $\mathbf{P^{Msink}_{med}}$ simulation, eight other simulations have then been run using a dissolution rate and a sinking speed for the PFe_{Inorg} covering 3 orders of magnitude. Indeed, for each dissolution rate (i.e., P_{min}, P_{med}, and P_{slem}; see Table 2), three different sinking speed of PFe_{Inorg} have been tested (i.e., no sinking, 0.2 and 2 m/day). The resulting iron inventories are detailed in Table 4.

From these results, the dissolution rate appears to be the most important parameter driving the total iron inventory with the smallest values obtained with the highest dissolution rate (e.g., P_{slem}, with any value of the vertical sinking speed). In the simulations using a high dissolution rate (P_{slem}), the fast PFe_{Inorg} dissolution explains its low concentration that reflects on the total iron inventory (indeed, this PFe_{Inorg} low concentration is not compensated by a mirroring increase in the DFe inventory due to significant scavenging). Moreover, when the dissolution rate is high, the vertical sinking speed does not represent a substantial PFe_{Inorg} sink, relatively to the dissolution, and therefore, it does not alter in any significant way the simulated iron budgets.

Conversely, simulations performed with a low dissolution rate, as in P_{min} simulations, displays the highest total iron inventory. This high total iron inventory is explained by the high concentrations of PFe_{Inorg} that represents between 46% ($\mathbf{P^{10sink}_{min}}$) and 93% ($\mathbf{P^{Nosink}_{min}}$) of total iron, while in any of the P_{slem} simulations this relative contribution does not exceed 11%. As expected, a low dissolution rate allows the added PFe_{Inorg} to remain longer in the ocean and thus, to more efficiently accumulate. In those low dissolution rate simulations, changes in the vertical sinking speed impact strongly the total iron inventory (even though it always is higher in P_{min} than in P_{slem} simulations) through its direct effect on the PFe_{Inorg} pool.

Concerning the DFe inventory, it varies noticeably less than the total iron and the particulate iron inventories. As already mentioned, iron scavenging prevents very effectively the iron concentration to increase beyond 0.7 nM. Therefore, a significant part of the iron that is released by the dissolution of PFe_{Inorg}, is rapidly lost by scavenging, especially in the intermediate and deep ocean, where DFe concentrations are close to this 0.7-nM threshold. Nevertheless, the DFe inventory can change up to 30% relative to $\mathbf{P^{Msink}_{med}}$ (in comparison, the total iron inventory varies by a factor up to 7). DFe is especially influenced by the amount of PFe_{Inorg} available for dissolution. The more PFe_{Inorg} is present in the ocean, the higher the DFe inventory will be. In fact, the more the iron is transported far from its sources by escaping biological uptake and scavenging as in form of the PFe_{Inorg}, the more it reaches remote areas with originally lower DFe concentrations and thus is less susceptible to be scavenged right after its dissolution from particles. As expected, simulations with the highest PFe_{Inorg} concentrations (due to slow dissolution and slow sinking, as in $\mathbf{P^{Nosink}_{min}}$ or $\mathbf{P^{Nosink}_{med}}$) are displaying the highest DFe inventories. On the contrary, the lowest DFe inventory is obtained in simulation $\mathbf{P^{10sink}_{min}}$ in which PFe_{Inorg} is removed quickly from the ocean through vertical sedimentation without having the time to significantly dissolve. In P_{slem} simulations, fast dissolution rates result in fueling regions already Fe-replenished, thus favoring scavenging and explaining the relatively low impact of PFe_{Inorg} on the DFe inventory.

3.3.1. Sensitivity of Iron Distribution Toward the Dissolution Rate of Lithogenic Sediment Particles

In order to illustrate the sensitivity of the global horizontal distribution of DFe to the dissolution rates, we chose to focus on differences of $\mathbf{P^{Msink}_{min}}$ and $\mathbf{P^{Msink}_{slem}}$ with the simulation $\mathbf{P^{Msink}_{med}}$, in which both the dissolution rate and sinking have been set to intermediate values. The resulting global horizontal distribution of DFe is then shown in Figure 5. In the productive layer (0–100 m) and in reference to $\mathbf{P^{Msink}_{med}}$, a fast dissolution ($\mathbf{P^{Msink}_{slem}}$) produces higher DFe concentrations (Figure 5a) near the coasts. Indeed, faster dissolution leads to more PFe_{Inorg} dissolving locally before being transported toward the open ocean. Consequently, faster dissolution also causes less PFe_{Inorg} to reach the remote open ocean areas and noticeably the Antarctic Circumpolar Current (ACC), the North Atlantic Drift or the Kuroshio extension. This latter process explains the slightly negative DFe differences surface patterns between

Table 4
Iron Inventories for the Different Sensitivity Tests in 10^{11} mol

Simulations	Total Fe inventory	Inventory DFe				Inventory Total PFe				Inventory of PFe_{Inorg} (*% of total PFe*)			
	Global	Global	0–100 m	100–500 m	500–topography	Global	0–100 m	100–500 m	500–topography	Global	0–100 m	100–500 m	500–topography
P^{Nosink}_{min}	126.60	7.78	0.17	1.05	6.55	118.90	15.54	36.50	66.83	118.30 (99%)	15.51 (100%)	36.43 (100%)	66.35 (99%)
P^{Msink}_{min}	46.11	6.79	0.09	0.67	6.03	39.32	1.34	5.48	32.49	38.85 (99%)	1.32 (98%)	5.43 (99%)	32.09 (99%)
P^{10sink}_{min}	10.2	4.96	0.08	0.52	4.36	5.05	0.12	0.53	4.40	4.65 (92%)	0.10 (83%)	0.49 (92%)	4.06 (92%)
P^{Nosink}_{med}	19.84	7.17	0.20	1.02	5.95	12.67	3.78	4.28	4.61	12.10 (95%)	3.75 (99%)	4.20 (98%)	4.15 (90%)
P^{10sink}_{med}	10.15	6.03	0.09	0.59	5.34	4.12	0.12	0.51	3.50	3.68 (89%)	0.10 (83%)	0.46 (90%)	3.13 (89%)
P^{Nosink}_{slem}	7.65	6.31	0.17	0.77	5.37	1.35	0.42	0.29	0.64	0.85 (63%)	0.39 (93%)	0.23 (79%)	0.23 (36%)
P^{Msink}_{slem}	7.55	6.28	0.16	0.77	5.35	1.27	0.33	0.29	0.65	0.77 (61%)	0.30 (91%)	0.24 (83%)	0.24 (37%)
P^{10sink}_{slem}	7.54	6.17	0.11	0.73	5.33	1.37	0.10	0.27	1,00	0.89 (65%)	0.08 (80%)	0.22 (81%)	0.59 (59%)

Note. P_{slem}, P_{med}, and P_{min} correspond to dissolution rates of 6×10^{-3}, 4×10^{-4}, and 4×10^{-5} day, respectively, while labels "Nosink," "Msink," and "10sink" correspond, respectively, to no vertical sinking speed, 0.2 and 2 m/day (see Table 2 for details).

$\mathbf{P^{Msink}_{slem}}$ and $\mathbf{P^{Msink}_{med}}$. Conversely, low dissolution rate ($\mathbf{P^{Msink}_{min}}$; Figure 5c) translates to noticeably lower values of surface DFe concentrations near the coasts in reference to $\mathbf{P^{Msink}_{med}}$. Further away from the coastlines, surface DFe does not increase despite a PFe_{Inorg} increase (not shown). The PFe_{Inorg} increase does not compensate for the slow dissolution and $\mathbf{P^{Msink}_{med}}$ does simulate higher DFe in every places of the surface ocean (Figure 5c).

In subsurface and near the topography (Figure 5b), the differences between $\mathbf{P^{Msink}_{slem}}$ and $\mathbf{P^{Msink}_{med}}$ are noticeably weaker than in surface. Vertical attenuation of the PFe_{Inorg} source and the relatively slow subsurface circulation (compared to the surface) that allows for a large part the PFe_{Inorg} from $\mathbf{P^{Msink}_{med}}$ and $\mathbf{P^{Msink}_{slem}}$ to dissolve locally, close to the source regions near topography for both simulations, is explaining this pattern. Regions near topography, where higher DFe concentrations are simulated in $\mathbf{P^{Msink}_{slem}}$ than in $\mathbf{P^{Msink}_{med}}$, are the ones with the most intense subsurface circulation. In all other open ocean regions, the PFe_{Inorg} mostly released in surface layers is depleted faster in $\mathbf{P^{Msink}_{slem}}$ than in $\mathbf{P^{Msink}_{med}}$ resulting in weaker horizontal transport of PFe_{Inorg}, prone to dissolve, toward the subsurface through vertical sinking (below high PFe_{Inorg} surface concentration patterns; Figure 4 e) and through ocean transport in convergence zones (Figure 4f). Therefore, these patterns mostly represent the higher dissolution of the PFe_{Inorg} transported from the surface in $\mathbf{P^{Msink}_{med}}$. In $\mathbf{P^{Msink}_{min}}$, as in surface, the DFe is everywhere lower than in $\mathbf{P^{Msink}_{med}}$ in subsurface with patterns resembling the one of Figure 5b. Indeed, despite its high concentration, the very slow PFe_{Inorg} dissolution does not imprint the subsurface DFe concentration in $\mathbf{P^{Msink}_{min}}$, and the patterns displayed in Figure 5d are again related to the dissolution of the PFe_{Inorg} transported from the surface through ocean circulation in $\mathbf{P^{Msink}_{med}}$.

It is worth noting that high dissolution rates ($\mathbf{P^{Msink}_{slem}}$) tend to accentuate the observed coast to offshore DFe gradient by decreasing the PFe_{Inorg} ability to be transported far away from its source.

3.3.2. Sensitivity of Iron Distribution Toward the Sinking Velocity of Lithogenic Sediment Particles

The sinking speed parameterization is directly impacting the vertical export of PFe_{Inorg} from the surface. Nonsinking PFe_{Inorg} (Nosink simulations) remain longer in surface resulting in an overall higher dissolution of PFe_{Inorg} (Table 4). Conversely, fast sinking PFe_{Inorg} leads to a high export from the surface, and thus, less PFe_{Inorg} is available to dissolve (Table 4). This global process is particularly visible in regions with shallow bathymetry (Figure 6a; e.g., arctic ocean, Hudson Bay, and the Baltic sea). Nonsinking PFe_{Inorg} also follows the surface ocean circulation until fully dissolved, while fast sinking PFe_{Inorg} ($\mathbf{P^{10sink}_{med}}$) are not efficiently transported away from the source regions. Figure 6a shows that nonsinking PFe_{Inorg} is adding DFe in remote areas less accessible to the sinking PFe_{Inorg}. On the contrary, fast sinking PFe_{Inorg} ($\mathbf{P^{10sink}_{med}}$) affects the DFe in regions located upstream (therefore closer to the PFe_{Inorg} source regions in coastal areas; Figures 6a and 6c) but presents almost no DFe differences in reference to $\mathbf{P^{Msink}_{med}}$ in the most remote places of the ocean (e.g., subtropical gyres center). Interestingly, the surface Southern Ocean is

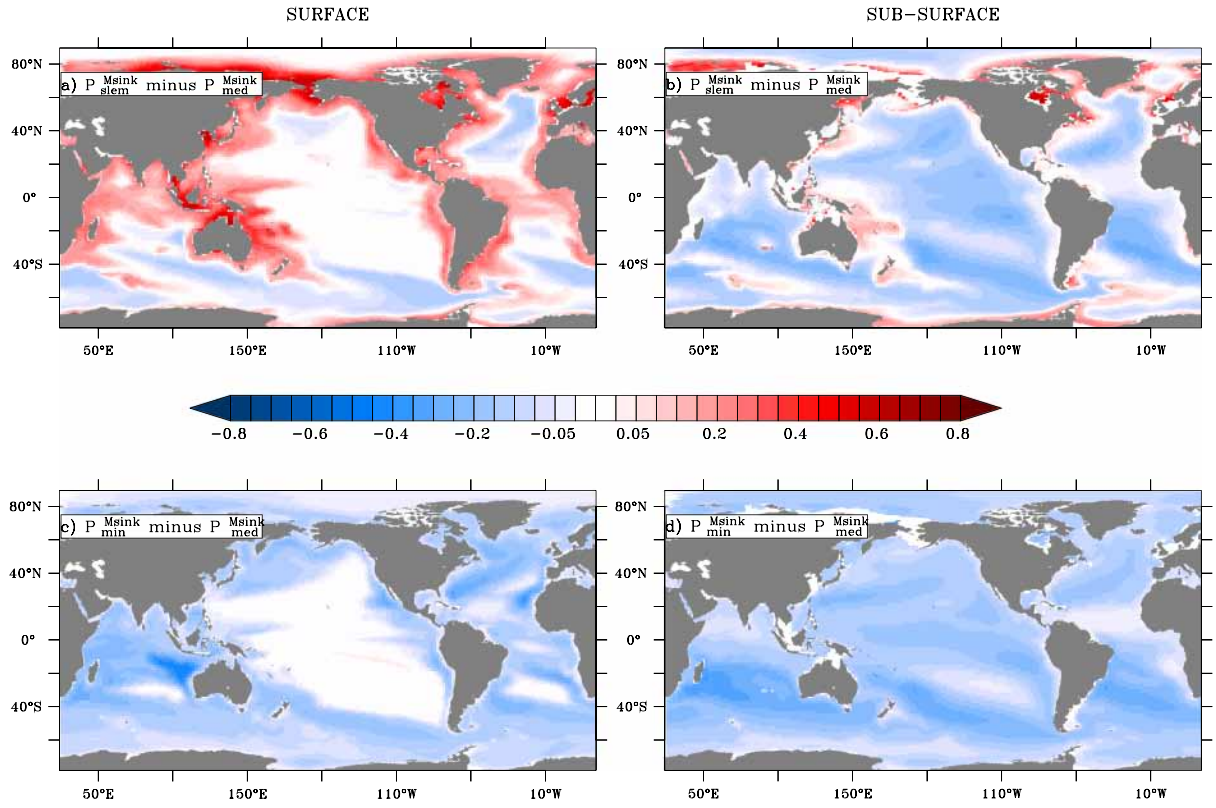

Figure 5. Differences of dissolved iron (in nmol/L) in reference to simulation $\mathbf{P^{Msink}_{med}}$ for (a and b) the simulation $\mathbf{P^{Msink}_{slem}}$, respectively, between 0–100 and 100–500 m. (c and d) Same as (a) and (b) but for $\mathbf{P^{Msink}_{min}}$ simulation.

showing almost no difference in DFe distributions between $\mathbf{P^{Nosink}_{med}}$ and $\mathbf{P^{Msink}_{med}}$ (Figure 6a). The very energetic and barotropic circumpolar circulation is dominating the spatial distribution of PFe_{Inorg} and therefore its relative contribution to the DFe pool, in $\mathbf{P^{Msink}_{med}}$ and $\mathbf{P^{Nosink}_{med}}$. By comparison, fast sinking PFe_{Inorg} distribution ($\mathbf{P^{10sink}_{med}}$) is more affected by the interplay between the ocean dynamical circulation and the sinking speed, resulting in less PFe_{Inorg} (and consequently DFe) reaching the convergence zones at 45°S.

In subsurface, slower PFe_{Inorg} sinking speed in $\mathbf{P^{Nosink}_{med}}$ than in $\mathbf{P^{Msink}_{med}}$ produces noticeably higher subsurface DFe concentration (Figure 6b) with the most marked differences located beneath the global convergence zones (Figure 4f). Indeed, as already noted, the slow PFe_{Inorg} sinking speed increases the PFe_{Inorg} surface concentrations in $\mathbf{P^{Nosink}_{med}}$ relatively to $\mathbf{P^{Msink}_{med}}$. Then, the PFe_{Inorg} is transported in higher quantity through the convergence zones to the subsurface where it continues to dissolve. Finally, very few subsurface regions display a decrease of DFe concentrations in $\mathbf{P^{Nosink}_{med}}$ relatively to $\mathbf{P^{Msink}_{med}}$. They are limited to regions located beneath the highest PFe_{Inorg} concentration in $\mathbf{P^{Msink}_{med}}$. In those regions, the vertical sinking of PFe_{Inorg} from the surface fuels a more intense subsurface dissolution in $\mathbf{P^{Msink}_{med}}$ than in $\mathbf{P^{Nosink}_{med}}$.

Conversely, higher PFe_{Inorg} sinking speeds in $\mathbf{P^{10sink}_{med}}$ decreases significantly the global concentration of the PFe_{Inorg} in the subsurface in comparison to $\mathbf{P^{Msink}_{med}}$ as shown in Table 4. PFe_{Inorg} stays less time in the subsurface layers (between 100 and 500 m) of all regions in $\mathbf{P^{10sink}_{med}}$ than in $\mathbf{P^{Msink}_{med}}$ (due to $\mathbf{P^{10sink}_{med}}$ high sinking velocity parameterization), which mechanically results in a lower amount of iron being dissolved from the PFe_{Inorg}. Therefore, patterns of Figure 6d are related to the PFe_{Inorg} that have more time to dissolve in $\mathbf{P^{Msink}_{med}}$ than in $\mathbf{P^{10sink}_{med}}$ while sinking from the surface high concentrations areas.

3.4. Impact on Phytoplankton

In this subsection, we focus our attention on the PFe_{Inorg} impacts on the global distribution of phytoplankton. Surface chlorophyll concentration is used as a proxy of the phytoplankton biomass.

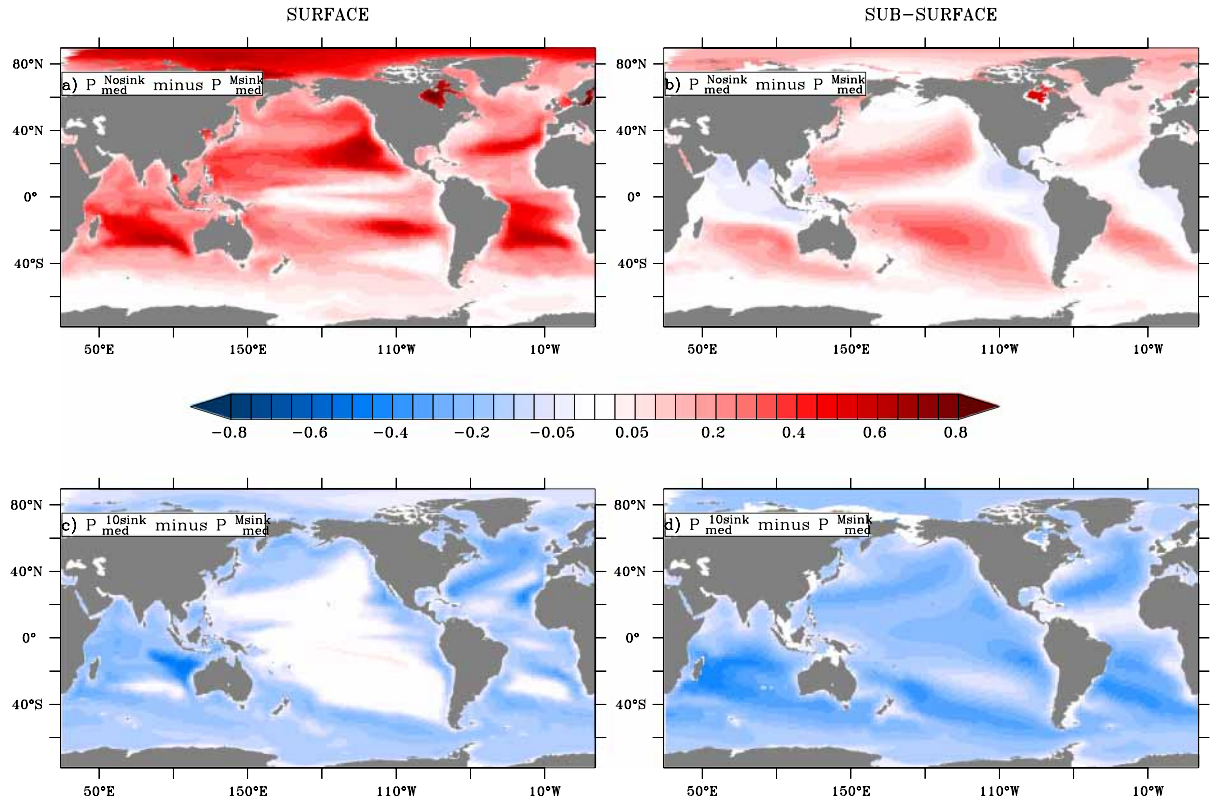

Figure 6. Spatial distribution differences of dissolved iron concentration (in nmol/L) averaged over the (left panel) first 100 m and (right panel) between 100- and 500-m depth.

As expected, surface chlorophyll concentration increases in all simulations where iron, in any form, is added relative to the D2 simulation (e.g., comparison between Figure 7a versus Figure 2b). Yet compared to a case where only a DFe source is considered from the sediments (Figure 7a), the $\mathbf{P^{Msink}_{med}}$ simulation shows an overall decrease in surface chlorophyll concentration in areas adjacent to the coastlines (including islands coastlines noticeable in Southern ocean). Further away from the coasts, the chlorophyll concentration is then significantly higher in the $\mathbf{P^{Msink}_{med}}$ simulation than in D10. These patterns are more noticeable in regions which are known to be iron limited such as the equatorial Pacific, the north Atlantic and Pacific (north of 40°N), and the Southern ocean (Moore et al., 2013). These changes of the chlorophyll distribution are, in most cases, consistent with the DFe alteration due to the PFe_{Inorg} (see Figure 4e and section 3.2).

Figure 8 focuses more specifically on three transects in contrasted regions of the world's ocean and highlights how their surface chlorophyll concentrations vary according to the addition of DFe, PFe_{Inorg}, and their parameterizations in the model. A comparison between these surface chlorophyll concentrations and the one observed (from SeaWiFS data) is given. Our simulations produce different chlorophyll background values that are blurring the impact of the PFe_{Inorg} on spatial chlorophyll distributions. Hence, we chose to normalize surface chlorophyll concentrations by the spatially averaged annual mean (Figure 8) over each transect.

Figures 8a and 8b are emphasizing the zonal and meridional gradients of the surface chlorophyll concentration in the equatorial Pacific. This region is characterized by a zonal transport of iron from the western Pacific subsurface to the eastern Pacific surface by the Equatorial Under Currents (Slemons et al., 2010, 2012). This iron is then brought to the surface by the equatorial upwelling in the eastern Pacific and partly fuels the phytoplankton growth. The corresponding SeaWiFS chlorophyll pattern is a steep zonal gradient centered around 170°W, which correspond to the transition between the cold tongue (cold upwelled water masses) and the oligotrophic warm pool (Figure 8a). Then, chlorophyll observed concentrations increase

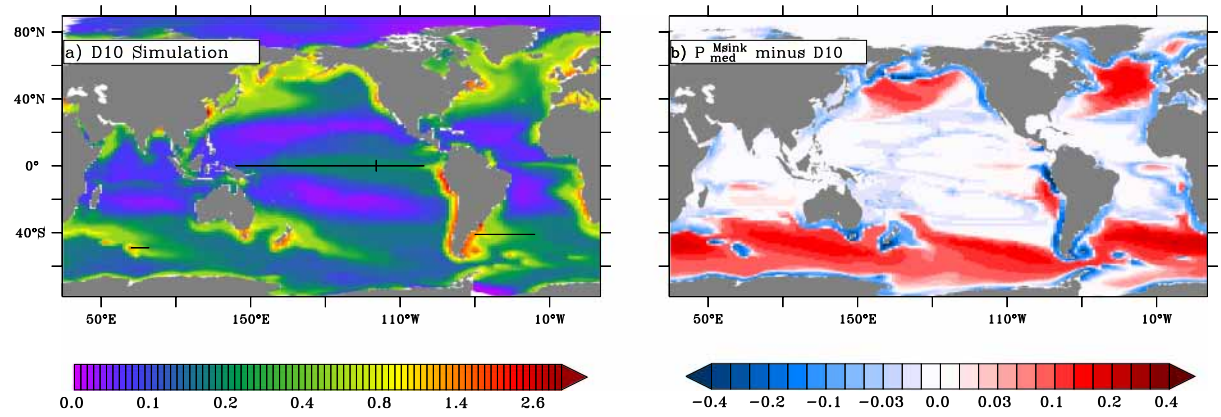

Figure 7. Annually averaged surface chlorophyll concentrations (in mg/m^3) for (a) the D10 simulation. Black lines mark the locations of the transects used in Figure 8. (b) The differences between $\mathbf{P^{Msink}_{med}}$ and D10 simulations in surface chlorophyll concentrations.

mildly toward the east before a steep increase in the far eastern equatorial Pacific (east of ~120°W). East of the international date line (180°), the simulations only considering sedimentary sources of DFe (i.e., D2 and D10) display significantly weaker eastward increase of chlorophyll concentrations (actually, almost constant concentration from 180° to 120°W) compared to the SeaWiFS data product. In the far east equatorial Pacific (east of 120°W), the latter simulations fail to reproduce the observed steep increase of chlorophyll concentrations.

Simulations in which PFe_{Inorg} has a small impact on surface DFe concentrations (i.e., simulations $\mathbf{P^{Msink}_{min}}$, $\mathbf{P^{10sink}_{min}}$, $\mathbf{P^{10sink}_{med}}$, and $\mathbf{P^{10sink}_{slem}}$; see Table 4) because of a relative high PFe_{Inorg} loss by sinking (and, for $\mathbf{P^{Msink}_{min}}$ a median sinking velocity but a weak dissolution rate), display similar features than the simulations taking into account only DFe concentrations. They underestimate the west-to-east surface chlorophyll gradient. On the contrary, simulations with the highest DFe inventories at the surface and in the subsurface ($\mathbf{P^{Nosink}_{min}}$ and $\mathbf{P^{Nosink}_{med}}$), due to relatively weak dissolution rates and a zero PFe_{Inorg} sinking speed, do not represent the steep chlorophyll increases near 170°E and east of 120°W. Those simulations also overestimate the west-to-east chlorophyll increase between 180° and 120°W. The simulations that perform the best in representing the surface chlorophyll west-to-east concentrations are those characterized by relatively high DFe surface inventory as well as relatively low subsurface DFe inventory: $\mathbf{P^{Msink}_{med}}$, $\mathbf{P^{Nosink}_{slem}}$, and $\mathbf{P^{Msink}_{slem}}$.

The latitudinal structure (at 130°W) of the observed equatorial Pacific (Figure 8b) surface chlorophyll concentrations displays a marked maximum centered around the equator with a steeper decrease to the north than to the south. Simulations that only account for a DFe sediment source underestimate the equatorial maximum and the chlorophyll drop north and south the equator resulting in an almost flat curve for the D2 simulated chlorophyll. D10 simulates a higher equatorial maximum but still underestimates the north and south chlorophyll decrease. As for the zonal gradient, simulations $\mathbf{P^{Msink}_{min}}$, $\mathbf{P^{10sink}_{min}}$, and $\mathbf{P^{10sink}_{med}}$ display chlorophyll concentrations close to D2, while $\mathbf{P^{10sink}_{slem}}$ simulated chlorophyll is closer to D10. Conversely, $\mathbf{P^{Nosink}_{min}}$ and $\mathbf{P^{Nosink}_{med}}$ simulations strongly overestimate the equatorial chlorophyll maximum and the northernmost surface chlorophyll decrease. Finally, the simulations $\mathbf{P^{Msink}_{med}}$, $\mathbf{P^{Nosink}_{slem}}$, and $\mathbf{P^{Msink}_{slem}}$ are able to better represent the observed marked maximum at the equator. This higher biomass of phytoplankton then deplete faster the nitrogen concentrations in the eastern Pacific equatorial region, leading to a lower meridional spread visible in Figure 8b as the north and south chlorophyll drop (also noticeable in Figure 7b).

In the Southern Ocean, we focused on the island mass effect produced by the Kerguelen archipelago. Indeed, the satellite surface chlorophyll data are displaying a chlorophyll plume downstream of the archipelago (Figures 7a and 8c) and iron fertilization has been invoked to explain such a remarkable feature (e.g., Blain et al., 2007). In this case, all our simulations are significantly overestimating the observed downstream chlorophyll decrease. In agreement with results found in the equatorial Pacific, simulations $\mathbf{P^{Msink}_{min}}$, $\mathbf{P^{10sink}_{min}}$, $\mathbf{P^{10sink}_{med}}$, and $\mathbf{P^{10sink}_{slem}}$ (characterized with low surface DFe inventories; see Table 4) are overestimating the most

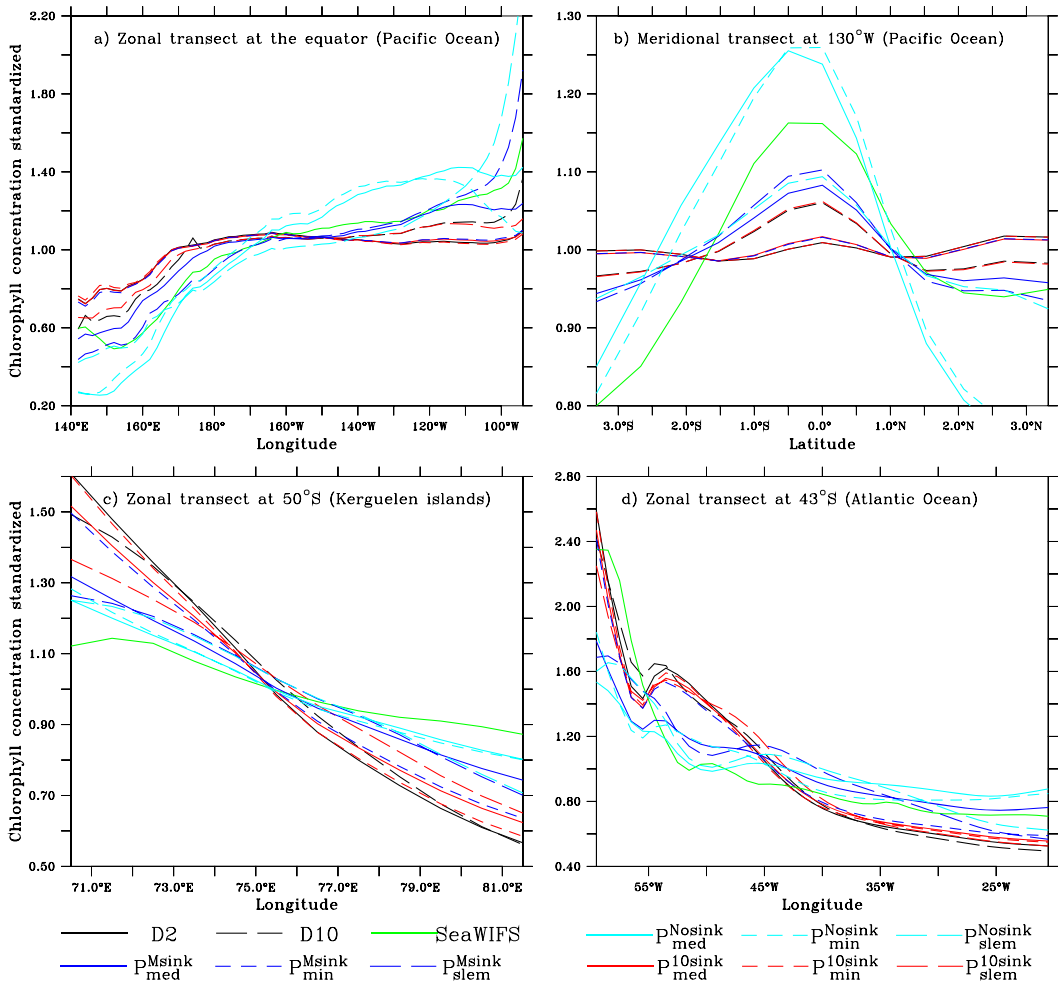

Figure 8. Annually averaged surface chlorophyll concentrations standardized by the spatially averaged annual mean chlorophyll concentrations along (a) a zonal transect at the equator in the Pacific Ocean (averaged from 1°N to 1°S), (b) a meridional transect at 130°W, (c) a zonal transect at the latitude of the Kerguelen islands (~50°S), and (d) a zonal transect at 43°S in the Atlantic ocean. Transects are represented by the black lines in Figure 8a.

the chlorophyll west-to-east decrease with concentrations close to the D2 and D10 simulations. A second group of simulations regroups $\mathbf{P^{Msink}_{med}}$, $\mathbf{P^{Nosink}_{slem}}$, and $\mathbf{P^{Msink}_{slem}}$. This latter group does represent a weaker downstream chlorophyll decrease, closer to the observed one. However, the best fit is obtained by simulations $\mathbf{P^{Nosink}_{min}}$ and $\mathbf{P^{Nosink}_{med}}$ that are representing too steep chlorophyll gradients in the equatorial Pacific (Figures 8a–8c).

In the Atlantic ocean we looked at the zonal gradient of chlorophyll near 43°S which corresponds to a strong zonal advection from the south American coast to the eastern Africa (Figure 4e). Observed chlorophyll concentrations display a marked maximum adjacent to the coast followed by a steep decrease from the coast to 53°W (Figure 8d). East of 53°W, chlorophyll concentrations decrease slowly with an almost linear trend. Here the simulations that take only DFe as sedimentary sources do a better job at representing the steep decrease chlorophyll west of 53°W while they are overestimating the chlorophyll zonal decrease east of this longitude. As for other plots in Figure 8, $\mathbf{P^{Msink}_{min}}$, $\mathbf{P^{10sink}_{min}}$, $\mathbf{P^{10sink}_{med}}$, and $\mathbf{P^{10sink}_{slem}}$ simulate similar chlorophyll decrease than D2 and D10. Conversely, the chlorophyll decreases simulated in $\mathbf{P^{Nosink}_{min}}$ and $\mathbf{P^{Nosink}_{med}}$ are too weak either west or east of 53°W. Finally, $\mathbf{P^{Msink}_{med}}$, $\mathbf{P^{Nosink}_{slem}}$, and $\mathbf{P^{Msink}_{slem}}$ are also displaying a slightly weaker than observed decrease in chlorophyll concentrations near the coast but they produce a more realistic zonal decrease in chlorophyll concentrations east of 53°W (the best fit to the observations being $\mathbf{P^{Msink}_{med}}$).

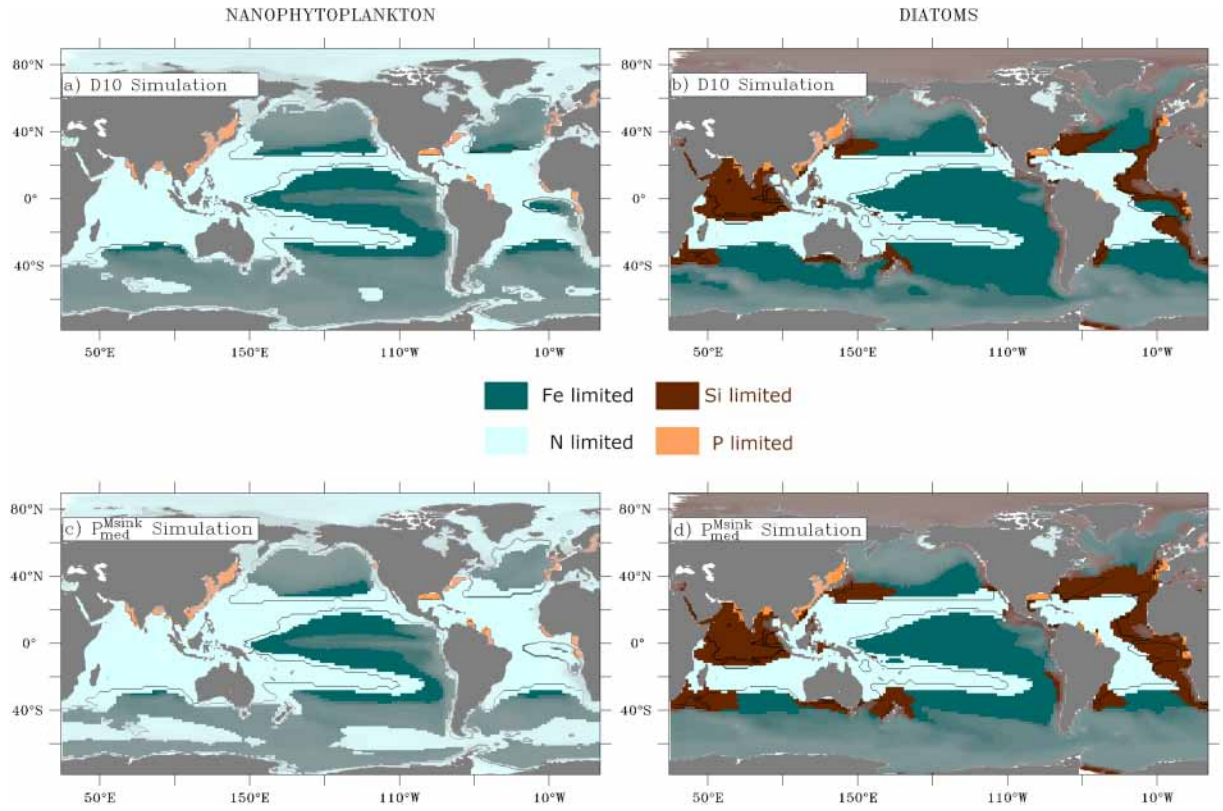

Figure 9. Limitation patterns of the surface nanophytoplankton growth during the boreal (North Hemisphere) and Southern (South Hemisphere) summer for (a) D10 and (c) $\mathbf{P^{Msink}_{med}}$. (b and d) Same as (a) and (c) but for limitation of the diatom growth. Contours in (a)–(d) delineate the same limitation regions but for D2. Shades of grey are given as an indicator of the level of total nutrients limitation (i.e., no shading = nutrient limited, dark grey = not nutrient limited).

A common impact of PFe_{Inorg} is then to change the spatial distribution of the phytoplankton biomass (diagnosed by the chlorophyll concentrations) in regions known to be iron limited (Figure 7b). A sediment source of PFe_{Inorg} is able to significantly change the coast to open ocean gradient as well as the Pacific equatorial upwelling meridional gradient in surface phytoplankton biomasses. All simulations considering only the DFe sediment source fail to simulate adequately those gradients (Figure 8) while our simulations $\mathbf{P^{Msink}_{med}}$, $\mathbf{P^{Nosink}_{slem}}$, and $\mathbf{P^{Msink}_{slem}}$ consistently improve the comparison to observations.

4. Conclusions and Perspectives

This first global modeling study is intended to document the potential impacts on dissolved iron and phytoplankton biomasses of an iron compartment increasingly considered as a key player in the ocean iron cycle but yet overlooked in biogeochemical models: the inorganic particulate iron of sedimentary origin (PFe_{Inorg}). In our study, we tested an increase of the dissolved iron source from sediments against an alternative: an iron source from the sediments that adds inorganic particulate iron to the dissolved one. Our results show that increasing the dissolved iron source by fivefold is less significant (see Table 3 and Figure 4) in terms of surface and subsurface impacts on the global inventory of dissolved iron than a change in the phase of the iron released by the sediments (i.e., particulate phase rather than dissolved). In turn, these results reflect on the surface phytoplankton biomasses that are most impacted by the addition of a particulate iron source (Figures 7–9) than increasing the dissolved one. Figure 9 shows that, contrary to an addition of PFe_{Inorg}, an increase of the sediment flux of dissolved iron only marginally changes the limitation patterns of the primary producers (Figures 9a and 9b).

These modeling results have been obtained using the most reasonable set of values for the model parameters. However, as our knowledge of this iron compartment is still relatively superficial, our modeling exercise relies on simplistic and poorly constrained parameterizations. Indeed, our simple model does represent

one source and two sinks, being the dissolution and the sinking of the PFe_{Inorg}. Our first modeling approach does not take into account the aggregation that has been shown to partially package small iron particles into large aggregates in productive surface waters (Ohnemus & Lam, 2015) and therefore may increase the mean vertical sinking speed of the PFe_{Inorg}. Our sensitivity tests using fast sinking PFe_{Inorg} are only partly addressing this process. Indeed, large aggregates have also been shown to break up in subsurface waters. Faster sinking due to aggregation in surface may result in low PFe_{Inorg} in surface ocean that should reflect on surface DFe. Low PFe_{Inorg} concentrations will then reach convergence zones and hence subsurface water masses. In other hand, fast sinking in surface with slow sinking in subsurface (related to de-aggregation) may drive an increase of PFeInorg in subsurface. Those two latter compensating processes do not have the same spatial imprint and spatial decoupling may affect the spatial patterns of the PFe_{Inorg} impact on DFe and biological production. Therefore, a parameterization of the vertical sinking speed that depends on biological productivity and depth may be needed in next PFe_{Inorg} modelization exercise. Another process that should be included in future studies would be an increased scavenging that an increased load of inorganic particles may generate in coastal waters. Indeed, iron oxyhydroxide particles are known for their high capacity of scavenging dissolved iron (Lam & Marchal, 2015; R. Raiswell & Anderson, 2005). Finally, the spatial and temporal variability of the sediment source, linked to the ocean dynamics, is not yet included in our modeling exercise.

Nevertheless, this simple parameterization relies on the very limited set of observations and laboratory experiments (Cheize et al., 2019) that are available and that can be used to constrain the model parameters. A noticeable assumption in our simulations is to set the dissolution rate to a constant and globally uniform value. Regional differences in the dominant types of sediment (Dutkiewicz et al., 2016) make this assumption very unlikely as Cheize et al. (2019) demonstrated differences in the dissolution kinetics of three types of sediment from very close locations (i.e., Kerguelen islands; Figure 3). One way to improve our parameterization would be to use regional dissolution rates. It would require to simulate several lithogenic iron compartments each from one type sediments and with distinctive dissolution rates. Characterization of the dissolution rates for each types of sediment present at global scale would then need to be gathered from experiments that have yet to take place. Moreover, the dependence of those dissolution rates to abiotic (e.g., light, temperature) and biotic (bacterial activity) environmental factors have to be assessed in order to refine the model. Indeed, those processes may explain the differences between the slow dissolution rates derived from the experimental data and the higher indirect estimation computed from in situ observations in Slemons et al. (2012).

This study does not aim at improving, at this stage of our knowledge, the simulated dissolved iron distribution through the addition of a PFe_{Inorg} compartment. Such a validation would require a global database distinguishing and quantifying for each sample the particulate iron from different origins (eolian, hydrothermal, sedimentary, or biogenic). These information are needed to provide a good comparison of the overall concentration of particulate iron that may result from a wrong combination of iron particles of different origins. Moreover, the PISCES global model has been optimized toward observations, without any PFe_{Inorg}, for more than a decade. Therefore, the addition of a PFe_{Inorg} compartment, which we know from observations are missing, will necessitate some future calibration in order to improve the model performance.

Finally, the lack of observations is an obvious concluding remark but is nonetheless crucial concerning the iron distribution in the ocean. Moreover, in situ observations alone are not sufficient to improve our understanding of the iron cycle and its impact on biogeochemical cycles. Therefore, the authors of this present study stress the need of tailored lab experiments designed in close collaboration between observationalists and modelers.

Acknowledgments
This work was supported by the CNRS LEFE-CYBER MOBIDIC, the ANR-BIIM (ANR-18-CE01-0006-01), and by the LabexMER (ANR-10-LABX-19-01) projects. The present work was also supported by the Instituto Milenio de Oceanografia (IMO-Chile), funded by the Iniciativa Cientifica Milenio (ICM-Chile), and by FONDECYT project 11160801 for P.A. Auger. Models outputs used in this study are available at http://data.umr-lops.fr/pub/Iron/PFEI.

References

Abadie, C., Lacan, F., Radic, A., Pradoux, C., & Poitrasson, F. (2017). Iron isotopes reveal distinct dissolved iron sources and pathways in the intermediate versus deep Southern Ocean. *Proceedings of the National Academy of Sciences*, *114*(5), 858–863. https://doi.org/10.1073/pnas.1603107114

Annett, A. L., Fitzsimmons, J. N., Séguret, M. J. M., Lagerström, M., Meredith, M. P., Schofield, O., & Sherrell, R. M. (2017). Controls on dissolved and particulate iron distributions in surface waters of the Western Antarctic Peninsula shelf. *Marine Chemistry*, *196*, 81–97. https://doi.org/10.1016/j.marchem.2017.06.004

Archer, D. E., & Johnson, K. (2000). A model of the iron cycle in the ocean. *Global Biogeochemical Cycles*, *14*(1), 269–279. https://doi.org/10.1002/(ISSN)1944-9224

Aumont, O., & Bopp, L. (2006). Globalizing results from ocean in situ iron fertilization studies. *Global Biogeochemical Cycles*, *20*, GB2017. https://doi.org/10.1029/2005GB002591

Aumont, O., Ethé, C., Tagliabue, A., Bopp, L., & Gehlen, M. (2015). PISCES-v2: an ocean biogeochemical model for carbon and ecosystem studies. *Geoscientific Model Development*, *8*(8), 2465–2513. https://doi.org/10.5194/gmd-8-2465-2015

Blain, S., Carlotti, F., Christaki, U., Corbiere, A., Durand, I., Ebersbach, F., et al. (2007). Effect of natural iron fertilization on carbon sequestration in the Southern Ocean. *Nature*, *446*, 1070–1074. https://doi.org/10.1038/nature05700

Borrione, I., Aumont, O., Nielsdóttir, M. C., & Schlitzer, R. (2014). Sedimentary and atmospheric sources of iron around South Georgia, Southern Ocean: A modelling perspective. *Biogeosciences*, *11*(7), 1981–2001. https://doi.org/10.5194/bg-11-1981-2014

Bowie, A. R., Van Der Merwe, P., Quéroué, F., Trull, T., Fourquez, M., Planchon, F., et al. (2015). Iron budgets for three distinct biogeochemical sites around the Kerguelen Archipelago (Southern Ocean) during the natural fertilisation study, KEOPS-2. *Biogeosciences*, *12*(14), 4421–4445. https://doi.org/10.5194/bg-12-4421-2015

Boyd, P. W., & Ellwood, M. J. (2010). The biogeochemical cycle of iron in the ocean. *Nature Geoscience*, *3*(10), 675–682. https://doi.org/10.1038/ngeo964

Buesseler, K. O., Andrews, J. E., Pike, S. M., & Charette, M. A. (2004). The Effects of Iron Fertilization on Carbon Sequestration in the Southern Ocean. *Science*, *304*(5669), 414–417. https://doi.org/10.1126/science.1086895

Chase, Z., Hales, B., Cowles, T., Schwartz, R., & van Geen, A. (2005). Distribution and variability of iron input to Oregon coastal waters during the upwelling season. *Journal of Geophysical Research*, *110*, C10S12. https://doi.org/10.1029/2004JC002590

Cheize, M., Planquette, H. F., Fitzsimmons, J. N., Pelleter, E., Sherrell, R. M., Lambert, C., et al. (2019). Contribution of resuspended sedimentary particles to dissolved iron and manganese in the ocean: An experimental study. *Chemical Geology*, *511*, 389–415. https://doi.org/10.1016/j.chemgeo.2018.10.003

Croot, P. L., & Hunter, K. A. (1998). Trace metal distributions across the continental shelf near Otago Peninsula, New Zealand. *Marine Chemistry*, *62*(3–4), 185–201. https://doi.org/10.1016/S0304-4203(98)00036-X

Da Cunha, L. C., & Buitenhuis, E. T. (2013). Riverine influence on the tropical atlantic ocean biogeochemistry. *Biogeosciences*, *10*(10), 6357–6373. https://doi.org/10.5194/bg-10-6357-2013

Dale, A. W., Nickelsen, L., Scholz, F., Hensen, C., Oschlies, A., & Wallmann, K. (2015). A revised global estimate of dissolved iron fluxes from marine sediments. *Global Biogeochemical Cycles*, *29*, 691–707. https://doi.org/10.1002/2014GB005017

Doty, M. S., & Oguri, M. (1956). The island mass effect. *ICES Journal of Marine Science*, *22*(1), 33–37. https://doi.org/10.1093/icesjms/22.1.33

Dutkiewicz, A., O'Callaghan, S., & Müller, R. D. (2016). Controls on the distribution of deep-sea sediments. *Geochemistry, Geophysics, Geosystems*, *17*, 3075–3098. https://doi.org/10.1002/2016GC006428

Dutkiewicz, S., Follows, M. J., & Parekh, P. (2005). Interactions of the iron and phosphorus cycles: A three-dimensional model study. *Global Biogeochemical Cycles*, *19*, GB1021. https://doi.org/10.1029/2004GB002342

Elrod, V. A., Berelson, W. M., Coale, K. H., & Johnson, K. S. (2004). The flux of iron from continental shelf sediments: A missing source for global budgets. *Geophysical Research Letters*, *31*, L12307. https://doi.org/10.1029/2004GL020216

Garcia, H. E., Locarnini, R. A., Boyer, T. P., Antonov, J. I., Bara-nova, O. K., Zweng, M. M., & Johnson, D. R. (2010). *World Ocean At-las 2009, Volume 4: Nutrients (Phosphate, Nitrate, Silicate)*, *Noaa Atlas Nesdis*, (71st ed.p. 398). Washington, DC: US Government Printing Office.

Geider, R. J., & La Roche, J. (1994). The role of iron in phytoplankton photosynthesis, and the potential for iron-limitation of primary productivity in the sea. *Photosynthesis Research*, *39*(3), 275–301. https://doi.org/10.1007/BF00014588

Geider, R. J., MacIntyre, H. L., & Kana, T. M. (1997). Dynamic model of phytoplankton growth and acclimation: Responses of the balanced growth rate and the chlorophyll a:carbon ratio to light, nutrient-limitation and temperature. *Marine Ecology Progress Series*, *148*(1–3), 187–200. https://doi.org/10.3354/meps148187

Gorgues, T., Menkes, C., Aumont, O., Slemons, L., & Murray, J. (2009). The iron phases, a crucial factor for the biomass variability in the Pacific HNLC region ?

Gorgues, T., Menkes, C., Slemons, L., Aumont, O., Dandonneau, Y., Radenac, M. H., et al. (2010). Revisiting the La Niña 1998 phytoplankton blooms in the equatorial Pacific. *Deep-Sea Research Part I: Oceanographic Research Papers*, *57*(4), 567–576. https://doi.org/10.1016/j.dsr.2009.12.008

Gourain, A., Planquette, H., Cheize, M., & Lemaitre, N. (2018). Inputs and processes affecting the distribution of particulate iron in the North Atlantic along the GEOVIDE (GEOTRACES GA01) section. *Biogeosciences Discussions*, *16*(7), 1563–1582. https://doi.org/10.5194/bg-2018-234

Hare, C. E., DiTullio, G. R., Trick, C. G., Wilhelm, S. W., Bruland, K. W., Rue, E. L., & Hutchins, D. A. (2005). Phytoplankton community structure changes following simulated upwelled iron inputs in the Peru upwelling region. *Aquatic Microbial Ecology*, *38*(3), 269–282. https://doi.org/10.3354/ame038269

Homoky, W. B., John, S. G., Conway, T. M., & Mills, R. A. (2013). Distinct iron isotopic signatures and supply from marine sediment dissolution. *Nature Communications*, *4*(1), 2143. https://doi.org/10.1038/ncomms3143

Honeyman, B. D., & Santschi, P. H. (1989). A Brownian-pumping model for oceanic trace metal scavenging: Evidence from Th isotopes. *Journal of Marine Research*, *47*(4), 951–992. https://doi.org/10.1357/002224089785076091

Hutchins, D. A., Hare, C. E., Weaver, R. S., Zhang, Y., Firme, G. F., DiTullio, G. R., et al. (2002). Phytoplankton iron limitation in the Humboldt Current and Peru Upwelling. *Limnology and Oceanography*, *47*(4), 997–1011. https://doi.org/10.4319/lo.2002.47.4.0997/full

Jeandel, C., & Oelkers, E. H. (2015, February). The influence of terrigenous particulate material dissolution on ocean chemistry and global element cycles. *Chemical Geology*, *395*, 50–66. https://doi.org/10.1016/j.chemgeo.2014.12.001

Jeandel, C., Peucker-Ehrenbrink, B., Jones, M. T., Pearce, C. R., Oelkers, E. H., Godderis, Y., et al. (2011). Ocean margins: The missing term in oceanic element budgets? *Eos*, *92*(26), 217–218. https://doi.org/10.1029/2011EO260001

Jickells, T. D. (2005). Global Iron Connections Between Desert Dust, Ocean Biogeochemistry, and Climate. *Science*, *308*(5718), 67–71. https://doi.org/10.1126/science.1105959

Johnson, K. S., Chavez, F. P., & Friederich, G. E. (1999). Continental-shelf sediment as a primary source of iron for coastal phytoplankton The availability of iron, an essential nutrient, controls rates of phytoplankton primary productivity in the open-ocean, upwel- ling ecosystems of the equatorial Paci®c. Retrieved from https://www3.mbari.org/chemsensor/papers/johnson_cont_shelf_fe.pdf

Johnson, K. S., Gordon, R. M., & Coale, K. H. (1997). What controls dissolved iron concentrations in the world ocean? *Marine Chemistry*, *57*(3–4), 137–161. https://doi.org/10.1016/S0304-4203(97)00043-1

Labatut, M., Lacan, F., Pradoux, C., Chmeleff, J., Radic, A., Murray, J. W., et al. (2014). Iron sources and dissolved-particulate interactions in the seawater of the Western Equatorial Pacific, iron isotope perspectives. *Global Biogeochemical Cycles*, *28*, 1044–1065. https://doi.org/10.1002/2014GB004928

Lam, P. J., & Bishop, J. K. B. (2008). The continental margin is a key source of iron to the HNLC North Pacific Ocean. *Geophysical Research Letters*, *35*, L07608. https://doi.org/10.1029/2008GL033294

Lam, P. J., Bishop, J. K. B., Henning, C. C., Marcus, M. A., Waychunas, G. A., & Fung, I. Y. (2006). Wintertime phytoplankton bloom in the subarctic Pacific supported by continental margin iron. *Global Biogeochemical Cycles*, *20*, GB1006. https://doi.org/10.1029/2005GB002557

Lam, P. J., & Marchal, O. (2015). Insights into Particle Cycling from Thorium and Particle Data. *Annual Review of Marine Science*, *7*(1), 159–184. https://doi.org/10.1146/annurev-marine-010814-015623

Lam, P. J., Ohnemus, D. C., & Marcus, M. A. (2012). The speciation of marine particulate iron adjacent to active and passive continental margins. *Geochimica et Cosmochimica Acta*, *80*, 108–124. https://doi.org/10.1016/j.gca.2011.11.044

Madec, G. (2008). *NEMO Ocean Engine, Note du Pôle de Modélisation 27* (Vol. 27). France: Institut Pierre-Simon Laplace (IPSL).

Middelburg, J. J., Soetaert, K., Herman, P. M. J., & Heip, C. H. R. (1996). Denitrification in marine sediments: A model study. *Global Biogeochemical Cycles*, *10*(4), 661–673. https://doi.org/10.1029/96GB02562

Milne, A., Schlosser, C., Wake, B. D., Achterberg, E. P., Chance, R., Baker, A. R., et al. (2017). Particulate phases are key in controlling dissolved iron concentrations in the (sub)tropical North Atlantic: Particulate Phases Control dFe. *Geophysical Research Letters*, *44*, 2377–2387. https://doi.org/10.1002/2016GL072314

Moore, C. M., Mills, M. M., Arrigo, K. R., Berman-Frank, I., Bopp, L., Boyd, P. W., et al. (2013). Processes and patterns of oceanic nutrient limitation. *Nature Geoscience*, *6*(9), 701–710. https://doi.org/10.1038/ngeo1765

Moore, J. K., & Braucher, O. (2008). Sedimentary and mineral dust sources of dissolved iron to the world ocean. *Biogeosciences*, *5*(3), 631. Retrieved from–656. www.biogeosciences.net/5/631/2008/, https://doi.org/10.5194/bg-5-631-2008

Moore, J. K., Doney, S. C., Glover, D. M., & Fung, I. Y. (2002). Iron cycling and nutrient-limitation patterns in surface waters of the world ocean. *Deep-Sea Research Part II: Topical Studies in Oceanography*, *49*(1–3), 463–507. https://doi.org/10.1016/S0967-0645(01)00109-6

Moore, J. K., Doney, S. C., & Lindsay, K. (2004). Upper ocean ecosystem dynamics and iron cycling in a global three-dimensional model. *Global Biogeochemical Cycles*, *18*, GB4028. https://doi.org/10.1029/2004GB002220

Ohnemus, D. C., & Lam, P. J. (2015). Cycling of lithogenic marine particles in the US GEOTRACES North Atlantic transect. *Deep Sea Research Part II: Topical Studies in Oceanography*, *116*, 283–302. https://doi.org/10.1016/j.dsr2.2014.11.019

Orr, J. C. (1999). On ocean carbon-cycle model comparison. *Tellus Series B: Chemical and Physical Meteorology*, *51*(2), 509–510. https://doi.org/10.3402/tellusb.v51i2.16334

Parekh, P., Follows, M. J., & Boyle, E. (2004). Modeling the global ocean iron cycle. *Global Biogeochemical Cycles*, *18*, GB1002. https://doi.org/10.1029/2003GB002061

Planquette, H., Fones, G. R., Statham, P. J., & Morris, P. J. (2009). Origin of iron and aluminium in large particles (> 53 μm) in the Crozet region, Southern Ocean. *Marine Chemistry*, *115*(1–2), 31–42. https://doi.org/10.1016/j.marchem.2009.06.002

Planquette, H., Sanders, R. R., Statham, P. J., Morris, P. J., & Fones, G. R. (2011). Fluxes of particulate iron from the upper ocean around the Crozet Islands: A naturally iron-fertilized environment in the Southern Ocean. *Global Biogeochemical Cycles*, *25*, GB2011. https://doi.org/10.1029/2010GB003789

Planquette, H., Sherrell, R. M., Stammerjohn, S., & Field, M. P. (2013). Particulate iron delivery to the water column of the Amundsen Sea, Antarctica. *Marine Chemistry*, *153*, 15–30. https://doi.org/10.1016/j.marchem.2013.04.006

Planquette, H., Statham, P. J., Fones, G. R., Charette, M. A., Moore, C. M., Salter, I., et al. (2007). Dissolved iron in the vicinity of the Crozet Islands, Southern Ocean. *Deep Sea Research Part II: Topical Studies in Oceanography*, *54*(18–20), 1999–2019. https://doi.org/10.1016/j.dsr2.2007.06.019

Raiswell, R., & Anderson, T. F. (2005). Reactive iron enrichment in sediments deposited beneath euxinic bottom waters: constraints on supply by shelf recycling. *Geological Society, London, Special Publications*, *248*(1), 179–194. https://doi.org/10.1144/GSL.SP.2005.248.01.10

Raiswell, R., & Canfield, D. E. (2012). The Iron Biogeochemical Cycle Past and Present. *Geochemical Perspectives*, *1*(1), 1–220. https://doi.org/10.7185/geochempersp.1.1

Slemons, L., Gorgues, T., Aumont, O., Menkes, C., & Murray, J. W. (2009). Biogeochemical impact of a model western iron source in the Pacific Equatorial Undercurrent. *Deep-Sea Research Part I: Oceanographic Research Papers*, *56*(12), 2115–2128. https://doi.org/10.1016/j.dsr.2009.08.005

Slemons, L., Paul, B., Resing, J., & Murray, J. W. (2012). Particulate iron, aluminum, and manganese in the Pacific equatorial undercurrent and low latitude western boundary current sources. *Marine Chemistry*, *142-144*, 54–67. https://doi.org/10.1016/j.marchem.2012.08.003

Slemons, L. O., Murray, J. W., Resing, J., Paul, B., & Dutrieux, P. (2010). Western Pacific coastal sources of iron, manganese, and aluminum to the EquatorialUndercurrent. *Global Biogeochemical Cycles*, *24*, GB3024. https://doi.org/10.1029/2009/GB003693

Smetacek, V., Klaas, C., Strass, V. H., Assmy, P., Montresor, M., Cisewski, B., et al. (2012). Deep carbon export from a Southern Ocean iron-fertilized diatom bloom. *Nature*, *487*(7407), 313–319. https://doi.org/10.1038/nature11229

Tagliabue, A., Aumont, O., Death, R., Dunne, J. P., Dutkiewicz, S., Galbraith, E., et al. (2016). How well do global ocean biogeochemistry models simulate dissolved iron distributions? *Global Biogeochemical Cycles*, *30*, 149–174. https://doi.org/10.1002/2015GB005289

Tagliabue, A., Bopp, L., Aumont, O., & Arrigo, K. R. (2009). Influence of light and temperature on the marine iron cycle: From theoretical to global modeling. *Global Biogeochemical Cycles*, *23*, GB2017. https://doi.org/10.1029/2008GB003214

Tagliabue, A., Bopp, L., Dutay, J. C., Bowie, A. R., Chever, F., Jean-Baptiste, P., et al. (2010). Hydrothermal contribution to the oceanic dissolved iron inventory. *Nature Geoscience*, *3*(4), 252–256. https://doi.org/10.1038/ngeo818

Tagliabue, A., Mtshali, T., Aumont, O., Bowie, A. R., Klunder, M. B., Roychoudhury, A. N., & Swart, S. (2012). A global compilation of dissolved iron measurements: focus on distributions and processes in the Southern Ocean. *Biogeosciences*, *9*(6), 2333–2349. https://doi.org/10.5194/bg-9-2333-2012

Tagliabue, A., Williams, R. G., Rogan, N., Achterberg, E. P., & Boyd, P. W. (2014). A ventilation-based framework to explain the regeneration-scavenging balance of iron in the ocean. *Geophysical Research Letters*, *41*, 7227–7236. https://doi.org/10.1002/2014GL061066

Van Der Merwe, P., Bowie, A. R., Quéroué, F., Armand, L., Blain, S., Chever, F., et al. (2015). Sourcing the iron in the naturally fertilised bloom around the Kerguelen Plateau: Particulate trace metal dynamics. *Biogeosciences*, *12*(3), 739–755. https://doi.org/10.5194/bg-12-739-2015

Ye, Y., Völker, C., & Wolf-Gladrow, D. A. (2009). A model of Fe speciation and biogeochemistry at the Tropical Eastern North Atlantic Time-Series Observatory site. *Biogeosciences*, *6*, 2041–2061. https://doi.org/10.5194/bg-6-2041-2009